https://doi.org/10.5194/acp-2021-279
Preprint. Discussion started: 26 April 2021

Atmospheric Chemistry and Physics Discussions

Radiative energy budget and cloud radiative forcing in the daytime marginal sea ice zone during Arctic spring and summer

Johannes Stapf[1], André Ehrlich[1], Christof Lüpkes[2], and Manfred Wendisch[1]

[1]Leipzig Institute for Meteorology (LIM), University of Leipzig, Germany
[2]Alfred Wegener Institute, Helmholtz Centre for Polar and Marine Research, Bremerhaven, Germany

Correspondence: Johannes Stapf (johannes.stapf@uni-leipzig.de)

Abstract. Airborne measurements of the surface radiative energy budget (REB) collected in the area of the marginal sea ice zone (MIZ) close to Svalbard (Norway) during two campaigns conducted in early spring and and early summer are presented. From the data, the cloud radiative forcing (CRF) was derived. The analysis is focussed on the impact of changing atmospheric thermodynamic conditions on the REB and on the linkage of sea ice properties and CRF. The observed two-mode longwave net irradiance frequency distributions above sea ice are compared with measurements from previous studies. The transition of both states (cloudy and cloud-free) from winter towards summer and the associated broadening of the modes is discussed as a function of the seasonal thermodynamic profiles and the surface type. The influence of cold air outbreaks (CAO) and warm air intrusions on the REB is illustrated for several case studies, whereby the source and sink terms of REB in the evolving CAO boundary layer are quantified. Furthermore, the role of thermodynamic profiles and the vertical location of clouds during on-ice flow is illustrated. The sea ice concentration was identified as the main driver of the shortwave cooling by the clouds. The longwave warming of clouds, estimated to about 75 $\mathrm{W\,m^{-2}}$, seems to be representative for this region, as compared to other studies. Simplified radiative transfer simulations of the frequently observed low-level boundary layer clouds and average thermodynamic profiles represent the observed radiative quantities fairly well. The simulations illustrate the delicate interplay of surface and cloud properties that modify the REB and CRF, and the challenges in quantifying trends in the Arctic REB induced by potential changes of the cloud optical thickness.

1 Introduction

The Arctic climate has experienced drastic transformations in the last decades (Meier et al., 2014; Koenigk et al., 2020), caused by global climate change and related uncertainty of local and remote feedback mechanisms (Goosse et al., 2018). One of the obvious Arctic climate changes is the amplified warming relative to the global warming (Wendisch et al., 2017), which is commonly referred to as Arctic amplification. Also, the diminishing sea ice extent (Stroeve and Notz, 2018) represents a dramatic climate change in the Arctic, playing a decisive role (Screens and Simmonds, 2010) in Arctic amplification via

https://doi.org/10.5194/acp-2021-279
Preprint. Discussion started: 26 April 2021


Atmospheric Chemistry and Physics Discussions

the related surface-albedo feedback (Pithan and Mauritsen, 2014; Block et al., 2020). However, a quantitative estimate of the intertwined feedback mechanisms relies on the representation of complex physical processes in climate models in the Arctic environment.

Climate models show a spread in the projected cloud fraction and the seasonal cycle of surface albedo and they indicate that the sign of the cloud radiative forcing (CRF, a quantification of the radiative warming or cooling by clouds) depends on the individually modelled sea ice properties (Karlsson and Svensson, 2013). The comparison of the rarely observed surface energy budget (SEB) in the inner Arctic with results of global reanalysis (Graham et al., 2019) and regional climate models (Pithan et al., 2014; Sedlar et al., 2020) indicate deficiencies in representing the SEB and the thermodynamic atmospheric structure in the Arctic. This emphasizes the importance of observations in the Arctic environment to improve model performance in this region.

Ground-based, long-term observations in the inner Arctic revealed two characteristic radiative and atmospheric thermodynamic winter states driven by the absence or presence of clouds and large scale processes (Stramler et al., 2011; Graham et al., 2017). Longwave net (downward minus upward) irradiances distributed around zero watts per meter squared are observed during periods of opaque Arctic low-level clouds with a cloud base temperature similar to the surface temperature. The second longwave radiative state distributed around -40 $\mathrm{W\,m^{-2}}$ (Stramler et al., 2011) represents cloud-free conditions, with a small downward longwave irradiance and a relatively warm surface. Seasonal changes in the atmospheric thermodynamic structure likely influence these two states and the impact of clouds on the radiative energy budget (REB) in the Arctic (Stapf et al., 2021).

With a decreasing sea ice concentration in the marginal sea ice zone (MIZ) towards the open ocean, the impact of clouds on the REB and the CRF changes due to the decreasing surface albedo, which enhances the shortwave cooling of clouds. Fitzpatrick and Warren (2007) quantified the impact of meridional changes of sea ice and clouds on the shortwave REB in the region of the Southern Ocean. They demonstrated that an increasing cloud optical thickness above the southern ocean relative to the conditions over sea ice might compensate for the effects of absence of sea ice in the summer-time surface REB. However, satellite observations of top of atmosphere albedo could not confirm these findings (Frey et al., 2018).

Above sea ice, the interplay of parameters relevant for the CRF, like microphysical and macrophysical cloud properties, solar zenith angle and surface albedo (Shupe and Intrieri, 2004) and the interaction of cloud and surface microphysical properties (Stapf et al., 2020) as well as the different interpretations and derivations of CRF (Stapf et al., 2021), make the quantification of the impact of clouds on the surface REB based on observations a challenge. Several studies have analysed and compared the saturation effect of the longwave CRF with increasing cloud optical thickness at different sites in the Arctic (Miller et al., 2015; Ebell et al., 2020). The atmospheric thermodynamic profiles likely play an important role in shaping the regional and seasonal longwave CRF (Cox et al., 2015; Stapf et al., 2021).

Except by local sea ice conditions and processes in the Arctic boundary layer, the REB is also driven by remote influences, such as large scale circulation patterns associated with warm air intrusions or cold air outbreaks (CAO) (Pithan et al., 2018). The North Atlantic represents one of the major transport pathways of warm and humid air masses into the Arctic (Mewes and Jacobi, 2019). This region is characterized by a high frequency of occurrence of CAOs, representing a crucial driver for a strong heat loss of the ocean and the generation of dense ocean waters relevant for ocean circulations (Papritz and Spengler,

https://doi.org/10.5194/acp-2021-279
Preprint. Discussion started: 26 April 2021


Atmospheric Chemistry and Physics Discussions

2017). CAOs have been studied extensively in airborne in situ observation to quantify the individual energy budget components (Brümmer, 1996, 1997), finding small and partly uncertain contributions of radiation to the boundary layer energy budget. In modelling studies of CAOs, radiative processes received less attention in the discussion of boundary layer evolution (Chechin and Lüpkes, 2017) or heat budget (Papritz and Spengler, 2017), though, these extreme conditions may also shape unique radiative characteristics. Warm air intrusions, on the other hand, are known to disturb the local SEB (Binder et al., 2017; Yamanouchi, 2019). Those events trigger large scale melting events over sea ice in summer (Tjernström et al., 2015) and influence the sea ice growth in winter (Persson et al., 2017). The thermodynamic transformation along the trajectories and the extent of moisture inversions is key to understand the consequences for the local REB (Tjernström et al., 2019).

Several airborne campaigns have been dedicated to the North Atlantic, the Fram Strait, and the MIZ northwest of Svalbard to study turbulence, radiation, and clouds (e.g., Hartmann et al., 1992; Brümmer, 1996; Wendisch et al., 2019), or investigate boundary layer processes (e.g., Lampert et al., 2012; Vihma et al., 2014; Tetzlaff et al., 2015) and air mass transformations during CAOs (e.g., Brümmer, 1996; Chechin et al., 2013). The MIZ represents a small area in the Arctic Ocean. Satellite observations have observed no general trend in MIZ extent, although their relative extent in summer increases (Rolph et al., 2020) due to a decreasing sea ice area in the Arctic and local trends such as those north of Svalbard (Tetzlaff et al., 2014). However, the MIZ is a crucial region to understand processes like thermodynamic adjustment of the atmosphere and cloud radiation interactions for different surface types, which helps to investigate potential changes in the future Arctic climate, especially in summer (Stroeve and Notz, 2018).

In this study, low-level airborne observations in the MIZ are presented to provide an overview of the specific characteristics of the REB and CRF in this dynamic region where sea ice, cloud, and thermodynamic conditions change on small spatial scales. The data were collected in the region northwest of Svalbard during two campaigns, the Arctic CLoud Observations Using airborne measurements during polar Day (ACLOUD) and the Airborne measurements of radiative and turbulent FLUXes of energy and momentum in the Arctic boundary layer (AFLUX) campaign. After an introduction of the dataset, a description of the observed conditions in the MIZ is given. Then we provide a characterization of mode structures of longwave net irradiances in cloud-free and cloudy conditions and their probable linkage to atmospheric thermodynamic conditions, season, and surface types in comparison to other available datasets. Case studies of warm air intrusions and CAOs are presented, discussing the impact of clouds on surface warming in relation to the vertical atmospheric structure and the possible radiative contributions to associated boundary layer transformation during CAOs. Considering the complex environment and statistical limitations, observations of CRF are extended and compared with radiative transfer simulations to illustrate the delicate interaction of parameters in shaping the REB and CRF in the environment of the MIZ.

2 Observations and radiative transfer simulations

2.1 Data basis and flights

During the ACLOUD campaign in May/June 2017, airborne observations have been conducted in the MIZ northwest of Svalbard. The scientific purpose and first results of the campaign were introduced by Wendisch et al. (2019). The synoptical

https://doi.org/10.5194/acp-2021-279
Preprint. Discussion started: 26 April 2021


Atmospheric Chemistry and Physics Discussions

overview of the campaign is given by (Knudsen et al., 2018). The instrumentation on board of both research aircraft Polar 5 and Polar 6 from the Alfred Wegener Institute (AWI) as well as the data processing is presented by Ehrlich et al. (2019b). In March/April 2019, the AFLUX campaign was performed in the same region as ACLOUD, using only the Polar 5 aircraft, but with identical remote sensing instrumentation. Between 21 March and 11 April 2019, 13 flights in the MIZ were accomplished with six hours of data in an altitude below 100 m (average 73 m), extending the 16 hours of low-level flights during ACLOUD (Stapf et al., 2020). Thus, both campaigns covered different seasons with late winter/early spring conditions during AFLUX (Section 3), and late spring/early summer conditions during ACLOUD, representing the transition from a cold season into a beginning warm melting season (Wendisch et al., 2019).

The basic instrumentation used in this study and the one by Stapf et al. (2020) has been operated during both campaigns. Broadband radiometer for upward and downward shortwave (0.2 - 4 $\mu\mathrm{m}$) and longwave (4 - 100 $\mu\mathrm{m}$) irradiance are used to quantify the REB with a frequency of 20 Hz. A 180° fish-eye camera is applied to derive the cosine-weighted sea ice fraction (I_f) and a Kelvin infrared-thermometer (KT-19) provides information on the surface brightness temperature. From dropsondes and aircraft in situ observations during ascents and descents in the vicinity of the low-level flight sections, the local atmospheric thermodynamic state and basic meteorological parameters are obtained. The cloud liquid water path (LWP) was derived during the below-cloud, low-level flights by a shortwave, transmissivity-based retrieval technique (Stapf et al., 2020). The retrieved values represent an equivalent LWP (assumed cloud droplet effective radius of 8 $\mu\mathrm{m}$), as cloud ice has not been considered in the simulations. In case of mixed-phase clouds, the retrieved values of equivalent LWP are lower compared to the real total water path (liquid plus ice).

2.2 Limitations of airborne radiation observations in the marginal sea ice zone

Due to the generally colder in-cloud temperatures during AFLUX, icing on the instruments was more likely compared to ACLOUD. Especially during longer horizontal flight sections in super-cooled cloud tops, occasionally sudden and persisting ice caps occurred on the glas domes of the pyranometers. The flat glas dome of the pyrgeometers were found to be iced less frequently. In cloudy and diffuse illuminated conditions, icing is difficult to detect and a possible influence on shortwave and longwave irradiances as discussed by Cox et al. (2021), can not fully be excluded. Nevertheless, during AFLUX about 21 % of the low-level shortwave irradiance measurements were discarded after quality checks using collocated radiative transfer simulations as well as manual tests of plausibility. During 5 % of the sections severe icing was observed, which also affected the longwave irradiances.

Due to a combination of slower true air speed in low-level sections (average of 56 $\mathrm{m\,s^{-1}}$ instead of 67 $\mathrm{m\,s^{-1}}$), more turbulent conditions, and a higher payload of the aircraft, the pitch angles have been slightly higher during AFLUX. Especially for high solar zenith angles (SZA) and optically thin clouds the alignment of the pyranometers fixed to the aircraft fuselage represents a major cause of uncertainty of airborne shortwave irradiance observations (Wendisch et al., 2001). The attitude threshold of the roll and pitch angles was increased from 4° to 5° compared to ACLOUD, but still, 28 % of the dataset had to be discarded. The combination of high SZA and thin clouds (sun disk visible) poses, without the ability to correct for the aircraft attitude like during cloud-free conditions (Ehrlich et al., 2019b), significantly higher uncertainties in shortwave irradiances, surface

https://doi.org/10.5194/acp-2021-279
Preprint. Discussion started: 26 April 2021


Atmospheric Chemistry and Physics Discussions

albedo, and retrieved LWP. Also, geometric issues arise for low sun conditions as the major information content for the LWP retrieval in these conditions (direct dominated irradiance), will be retrieved from larger horizontal distances to the actual point of observations. Furthermore, 3D effects of heterogeneous mid layer cloud fields occasionally introduced unreasonably high LWP values ($> 200\,\mathrm{g\,m^{-2}}$), which were consequently excluded from the analysis.

The airborne observations quantify the REB in flight altitude close to the ground, however, these values may differ from the surface REB depending on the atmospheric conditions. Especially over the open ocean and leads, sometimes differences between the air temperature in 60 m flight altitude and the surface temperature of up to 20 K occurred. In such cases, common during CAOs above water, radiative transfer simulations indicate a difference between cloud-free longwave net irradiances observed in flight altitude (60 m) and the ground of up to $10\,\mathrm{W\,m^{-2}}$. In case of strong surface temperature inversions over sea ice, up to $2\,\mathrm{W\,m^{-2}}$ difference is simulated. During AFLUX, the visibility during low-level flight sections was often reduced. Over leads and open water sea smoke developed and in the low boundary layer over sea ice, sometimes surface-based clouds or precipitation and also fog were observed, in contrast to the conditions observed during ACLOUD. These conditions can bias the longwave and shortwave irradiances and parameters such as surface albedo observed in flight altitude, but were not excluded because otherwise the typical springtime features of the MIZ as strong CAOs could not have been included in our analysis.

Another important aspect of this dataset is the temporal and spacial sampling. As the flights took place mostly during noon, the shortwave irradiance represents the maximum level during those days and does not hold for typical seasonal averaged shortwave irradiance conditions. The solar zenith angles (SZA) for AFLUX ranged between 72° and 82° degrees and would be representative for the daily range of SZA observed from end of April to the beginning of May. In addition, the flight operations were limited to suitable conditions for the Polar 5 and Polar 6 aircraft, which reduced, the number of warm air intrusion events during AFLUX significantly and, therefore, will bias the obtained distributions of radiative parameters.

Although these airborne radiation measurements are tainted with a higher uncertainty and limitations in temporal sampling compared to ground-based observations, they have the advantage to capture the continuously and quickly changing conditions in the MIZ of the Fram Strait with up to 3 m horizontal resolution on large horizontal scales with a flight speed of 50 to $70\,\mathrm{m\,s^{-1}}$.

2.3 Derivation of cloud radiative forcing and radiative transfer simulations

The gain or loss of energy of the surface due to radiation, the REB, can be derived from the individual components of net irradiances ($F_{\mathrm{net}} = F^{\downarrow} - F^{\uparrow}$) in the longwave and shortwave wavelength range:

$$F_{\mathrm{net}} = F_{\mathrm{net,sw}} + F_{\mathrm{net,lw}}. \tag{1}$$

To separately quantify the influence of clouds on the REB, the cloud radiative forcing (CRF, ΔF) after Ramanathan et al. (1989) is defined as the difference between shortwave and/or longwave net irradiances in cloudy ($F_{\mathrm{net,all}}$) and cloud-free conditions ($F_{\mathrm{net,cf}}$):

$$\Delta F = F_{\mathrm{net,all}} - F_{\mathrm{net,cf}}. \tag{2}$$

https://doi.org/10.5194/acp-2021-279
Preprint. Discussion started: 26 April 2021


Atmospheric Chemistry and Physics Discussions

The derivation of the CRF from airborne observations over homogeneous sea ice during the ACLOUD campaign using radiative transfer simulations for the required reference irradiances in cloud-free conditions is detailed in Stapf et al. (2020). This study extents the investigation by Stapf et al. (2020) to the entire MIZ including the open ocean. For the longwave CRF, two definitions of a radiative transfer-based estimate and an observation-based (climatological) CRF, discussed in Stapf et al. (2021), are used in this study. The challenge of calculating the shortwave CRF is to derive a surface albedo representative for cloud-free conditions, although the measurements are obtained in cloudy situations, whereby clouds influence the illumination conditions of the surface and consequently alter the surface albedo depending on the surface type.

The cloud-free albedo of homogeneous snow and ice surfaces $\alpha_{\mathrm{cf,snow/ice}}$ for I_f larger than 95 % is derived from observations in cloudy conditions by a retrieval detailed in Stapf et al. (2020). This approach is based on the combination of a snow albedo parameterization by Gardner and Sharp (2010) and the transmissivity-based retrieval of LWP that enables the continuous estimate of shortwave, cloud-free net irradiances.

Similarly, in this study, an estimate of the ocean surface albedo in cloud-free condition ($\alpha_{\mathrm{cf,w}}$) from cloudy observation is derived using the parameterization of Jin et al. (2011), which is applied over open ocean with a I_f below 5 %. Lookup tables of cloud-free, open ocean albedo have been produced in dependence of SZA, fraction of direction to diffuse incident irradiance, and wind speed; the influence of the chlorophyll content of the ocean is neglected. To extrapolate the wind speed at the surface from the observed one in flight altitude below 100 m, the logarithmic wind profile is used assuming neutral stability and a surface roughness of 0.0002 m above the open ocean. The required fraction of diffuse irradiance in cloud-free conditions is obtained from the radiative transfer simulations of downward shortwave irradiance, required for the CRF calculations. Details of the importance of various parameters controlling the open ocean albedo and its impact on the derived CRF are given in the Appendix A.

In the MIZ, the surface types of water and sea ice are mixed depending on the sea ice fraction. They strongly vary on small scales, consequently influencing the surface albedo and the CRF. By assuming a Lambertian surface albedo, the cosine-weighted sea ice fraction (I_f), obtained from fish-eye cameras, and its approximately linear relation to the albedo is used to weight the cloud-free, retrieved surface albedo of open ocean and sea ice:

$$\alpha_{\mathrm{cf}}(I_\mathrm{f}) = (\alpha_{\mathrm{cf,snow/ice}} - \alpha_{\mathrm{cf,w}}) \cdot I_\mathrm{f} + \alpha_{\mathrm{cf,w}}, \tag{3}$$

for I_f between 5 % and 95 %. Below and above these thresholds, a homogeneous surface was assumed to reduce uncertainties induced by misclassified surface types by the fish-eye camera images, like sea smoke or nilas. During AFLUX, the I_f might have been underestimated sometimes because dark nilas (ice) were incorrectly detected as water, which is relevant for the broadband surface albedo because dark nilas are characterized by different spectral reflection properties compared to open water (Zatko and Warren, 2015). Albedo values that exceed the ice fraction range between the albedo values of snow, ice and ocean, have been excluded from the analysis; they amount to 20 % and 12 % during AFLUX and ACLOUD. It needs to be considered that the full complexity of 3D radiative transfer in combination with mixtures of surface types in the MIZ can only imperfectly be described by the simplified assumption of a Lambertian surface.

https://doi.org/10.5194/acp-2021-279
Preprint. Discussion started: 26 April 2021

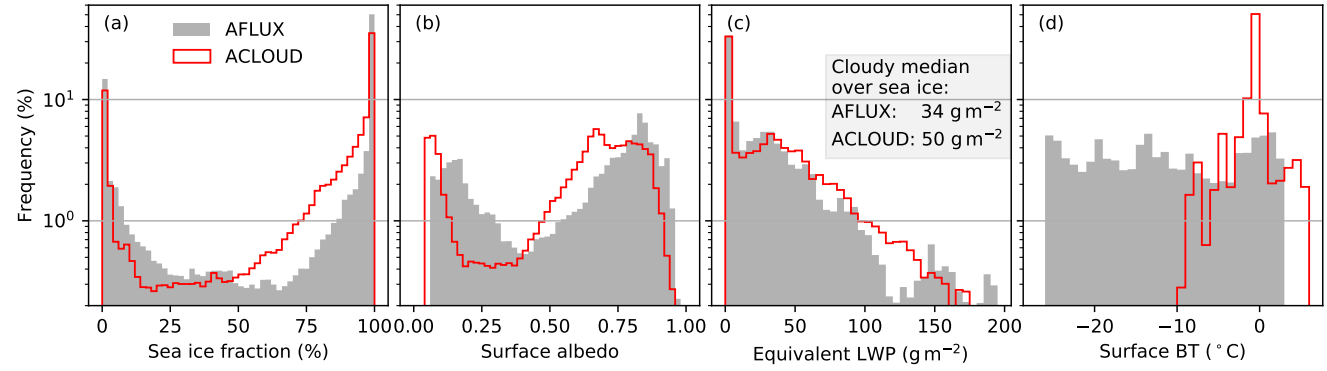

Figure 1. Histograms of observed and derived quantities during the AFLUX/ACLOUD low-level flights. Cosine weighted sea ice concentration (a), surface albedo in all-sky conditions (b), from shortwave transmissivity derived equivalent LWP (range limited to 200 g m^{-2}) (c), and surface brightness temperature (BT) (d).

The radiative transfer simulations were performed using the LibRadtran package (Emde et al., 2016) and are set up as described by Stapf et al. (2020). The local thermodynamic profiles obtained from dropsondes or in situ profiles measured by the aircraft were merged with upper air radiosoundings. During ACLOUD, radiosoundings from the Polarstern research vessel of the concurrent PASCAL campaign (Wendisch et al., 2019) in the MIZ northwest of Svalbard and the Ny-Ålesund research station (Svalbard) were used. During AFLUX, the information above approximately 3 km altitude were only available from Ny-Ålesund. This restriction results in slightly higher uncertainties of the simulated downward irradiances, especially with increasing distance from Ny-Ålesund.

3 Conditions in the marginal sea ice zone during the observations

3.1 Surface and cloud properties

Compared to ACLOUD, during AFLUX the sea ice edge (15 % isoline of satellite derived I_f) was situated, although earlier in the season, slightly further in the North, but still in reach of the aircraft. In Fig. 1a the frequency distributions of the sea ice concentration observed during all low-level flight legs of both campaigns are compared. Both data sets indicate that the majority of the low-level flights have been performed above homogeneous sea ice, while during ACLOUD a slightly higher fraction of flights were performed over fractional sea ice with concentrations between 50 % and 95 %. The corresponding distribution of the surface albedo is presented in Fig. 1b. The surface albedo distributions are determined by the sea ice distribution and show, similar to the sea ice fraction, bimodal shapes with slightly higher albedo values over sea ice during AFLUX compared to ACLOUD. The enhanced sea ice albedo earlier in the seasons results during cloud-free periods from higher solar zenith angles (SZA) of 72° to 82° during AFLUX compared to 55° to 69° during ACLOUD, but potentially also due to colder, and thus, fresher snow conditions with smaller snow grains. The ACLOUD distribution of surface albedo shows two slight sub-modes

https://doi.org/10.5194/acp-2021-279
Preprint. Discussion started: 26 April 2021


Atmospheric Chemistry and Physics Discussions

for sea ice (maxima at 0.6 and 0.76) due to the beginning melt season in the end of the campaign with decreasing surface albedo values. Also, the surface albedo of the open ocean is influenced by the different SZA of ACLOUD and AFLUX, which explains the broader open ocean albedo mode for AFLUX from 0.06 (cloudy) to 0.2 (cloud-free) compared to almost constant values below 0.1 for ACLOUD.

In Fig. 1c the frequency distribution of the retrieved equivalent LWP observed during both campaigns illustrates that during AFLUX cloud fields with an LWP below $30\,\mathrm{g\,m^{-2}}$ are more frequently observed compared to ACLOUD, where clouds with LWP above $30\,\mathrm{g\,m^{-2}}$ are slightly more often. The median LWP in cloudy conditions above sea ice (LWP > $5\,\mathrm{g\,m^{-2}}$, I_f > 95 %) amounts to $34\,\mathrm{g\,m^{-2}}$ for AFLUX and $50\,\mathrm{g\,m^{-2}}$ ACLOUD. During AFLUX, often thin and low cloud fields in a shallow boundary layer over sea ice were observed, as compared to ACLOUD with more homogeneous cloud fields in a boundary layer with larger vertical extent (Section 3.2). Nevertheless, in 80 % of the conditions, the LWP was lower than $58\,\mathrm{g\,m^{-2}}$ during AFLUX and $68\,\mathrm{g\,m^{-2}}$ during ACLOUD underlining the character of the frequent often thin low-level clouds in this region.

Conclusions of differences between clouds above open ocean and sea ice are not feasible because of the unreliable statistical evidence due to the daily cloud field variability and insufficient sampling of the flight pattern. The AFLUX LWP distribution shows a mode at over $150\,\mathrm{g\,m^{-2}}$, which can be partly addressed to one flight during a strong cold air outbreak with extraordinary optically thick clouds already above closed sea ice. Another characteristic difference between both campaigns represents the frequent presence of sea smoke and surface-based clouds during AFLUX, observed over open water leads embedded in the sea ice or during CAOs above the open ocean. Over sea ice, shallow fog-like conditions were observed more frequent during AFLUX as compared to ACLOUD, where mostly a clearly separated low cloud base was present with occasional precipitation. Due to lower cloud temperatures, also the cloud ice fraction should have been higher during AFLUX. Already the visual impression of collocated satellite images indicate that every flight/day represents different cloud properties and distributions of cloud fields driven by the large scale processes and have to be considered as highly variable during both campaigns.

3.2 Structure of the lower atmosphere

The different seasons are evident in the surface brightness temperature distributions shown in Fig. 1d. During AFLUX low surface temperatures of often below -20° C and surface temperature gradients in the MIZ of up to 25 K were found in the MIZ. The conditions were characterized by a strong daily variability of the surface temperatures depending on the synoptical situation (Section 3.3) and distribution of clouds in the area, but also more complex surface types like nilas (covered or uncovered by thin snow), which broadened the surface temperature distribution and underline the complexity of the surface in this region. Instead, during ACLOUD after a still cold period end of May, a thermodynamic rather uniform surface was observed in the beginning melt season in the MIZ, with surface temperatures distributed around the melting point of snow (see also Section 3.3).

Besides colder surface temperatures, the thermodynamic profiles show seasonal characteristics. In Fig. 2 the average temperature profiles over areas with a sea ice concentration above 90 % (derived from daily sea ice concentrations maps from Spreen et al., 2008) are shown along with long-term references from the Surface Heat Budget of the Arctic Ocean (SHEBA)

https://doi.org/10.5194/acp-2021-279
Preprint. Discussion started: 26 April 2021

Atmospheric Chemistry and Physics Discussions

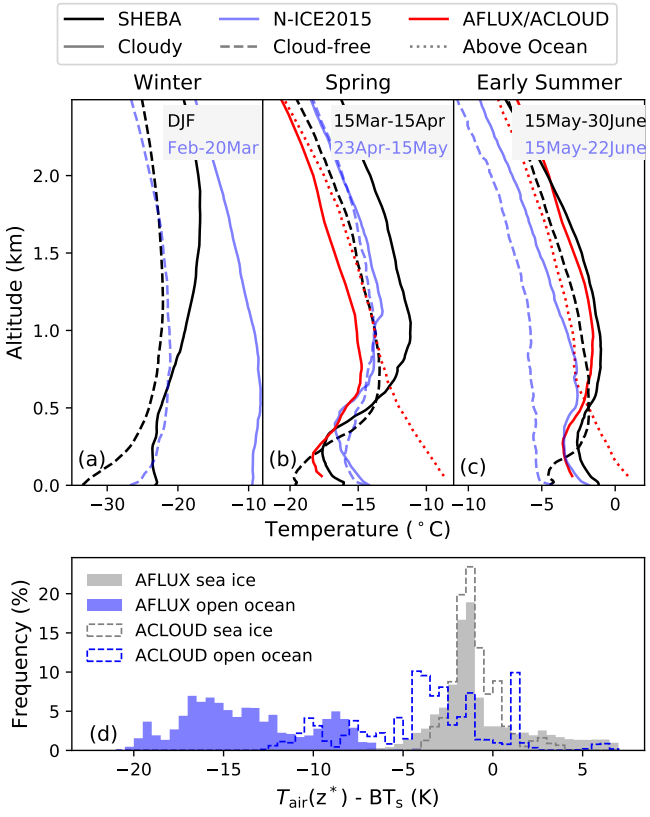

Figure 2. (a-c) Seasonal daily averaged temperature profiles observed during AFLUX/ACLOUD above sea ice and open ocean (all-sky conditions). Average SHEBA, and N-ICE2015 profiles separated by longwave net irradiances in cloudy (>-10 $\mathrm{W\,m^{-2}}$, N-ICE2015 spring >-20 $\mathrm{W\,m^{-2}}$) and cloud-free conditions (<-20 $\mathrm{W\,m^{-2}}$) for the time periods specified in the legend. (b) Temperature spread between air temperature in low-level flight altitude (z^*) and surface brightness temperature (negative meaning warmer surface). The ACLOUD histogram was daily weighted.

campaign (Uttal et al., 2002) (inner Arctic) and the Norwegian young sea ICE (N-ICE2015) campaign (Walden et al., 2017) (sea ice and MIZ north of Svalbard) for different seasons. Thermodynamic profiles and longwave net irradiances are used from Hudson et al. (2016) and Hudson et al. (2017) for N-ICE2015, and from Persson (2011) and Moritz (2017) for SHEBA. During ACLOUD, also Polarstern radiosoundings from the concurrent PASCAL campaign (Wendisch et al., 2019) in the sea ice area have been used. The aircraft observations are only shown above the minimum flight altitude due to the strong near-surface temperature variability discussed in Fig. 2d. A separation between cloudy and cloud-free profiles of AFLUX/ACLOUD appear unreliable due to insufficient statistics, and thus, is shown only for the SHEBA and N-ICE2015 campaigns.

During ACLOUD (spring/early summer), the average temperature profile is shaped by a frequently observed cloudy boundary layer with low-level clouds and a cloud top temperature inversion at altitudes between 300 and 400 m. This profile is in

https://doi.org/10.5194/acp-2021-279
Preprint. Discussion started: 26 April 2021


Atmospheric Chemistry and Physics Discussions

agreement with those observed in cloudy conditions during N-ICE2015 and SHEBA (slightly warmer) but differs in temperature inversion strength.

Compared to ACLOUD, a stronger temperature inversion above the even lower and approximately 15 K colder boundary layer was observed during AFLUX. Also, the near-surface lapse rate of the individual profiles depended more on the prevailing conditions over sea ice. They quickly adapted to the cloud conditions and transitioned between strong surface-based inversions in cloud-free conditions and more neutral profiles in cloudy situations (Stapf et al., 2021).

The profiles measured during N-ICE2015 are discussed by Cohen et al. (2017) and Kayser et al. (2017). For the time period of ACLOUD (Fig. 2c), they appear to have weaker cloud-top temperature inversions compared to ACLOUD. In cloud-free conditions they appear to be less stable compared to SHEBA (Fig. 2c). Kayser et al. (2017) illustrated (their Fig. 9) that in comparison to SHEBA, the near-surface layer tends to be more unstable during N-ICE2015. Cohen et al. (2017) (their Fig. 12) illustrates a less uniform transition of thermodynamic profiles from spring to summer, and a period of higher lifted inversion bases in cloudy and less stable cloud-free conditions during the April/May period in Fig. 2b. In late winter and early spring, N-ICE2015 profiles are (especially in the cloudy state) significantly warmer and less stable compared to SHEBA data due to strong synoptic storm events (Kayser et al., 2017; Cohen et al., 2017).

In addition to homogeneous sea ice, the average atmospheric profiles above open ocean are shown for AFLUX and ACLOUD. During both seasons the boundary layer height and temperature increases significantly towards the open ocean.

Fig. 2b provides a rough estimate of the near-surface stability for the different surface types open water and sea ice. Over homogeneous sea ice, the distributions of near-surface temperature spread indicate that the surface was warmer compared to the air above, distributed around values between -1 K and -2 K during both campaigns. These values represent mostly cloudy conditions with a neutral to slightly unstable near-surface layer. The occurence of thin nilas and likely also fluctuations of ice floe thickness caused sometimes strongly unstable near-surface layers even over sea ice with values up to -6 K. Surfaces with temperatures below the air temperatures in flight altitude and thus stably stratified surface layers were frequently observed during AFLUX in cloud-free conditions with strong, potentially surface-based inversions and a temperature spread of up to -7 K. During off-ice flows, cold air masses are advected above the warm open ocean causing strongly unstable conditions during AFLUX. During ACLOUD the temperature gradients were less extreme and only in the beginning of ACLOUD, CAOs induced temperature spreads up to around -10 K, while during less dynamic conditions moderate temperature spreads and even occasionally present surface-based inversions above the open ocean were found.

The broad distribution of near-surface stability between surface and atmosphere as well as the slightly unstable near-surface layer represents an interesting preconditioning relevant for the longwave net irradiances in this region.

3.3 Impact of synoptic scale processes

To identify the periods dominated by cold air outbreaks during both campaigns, in Fig. 3a the difference between potential skin temperature and potential temperature in 850 hPa (marine cold air outbreak index, MCAO), as commonly applied (e.g., Papritz and Spengler, 2017; Knudsen et al., 2018), were calculated from ERA5 reanalysis data (Hersbach et al., 2020). While during ACLOUD, Knudsen et al. (2018) identified three synoptic periods starting with a cold period with CAOs in May followed by

https://doi.org/10.5194/acp-2021-279
Preprint. Discussion started: 26 April 2021

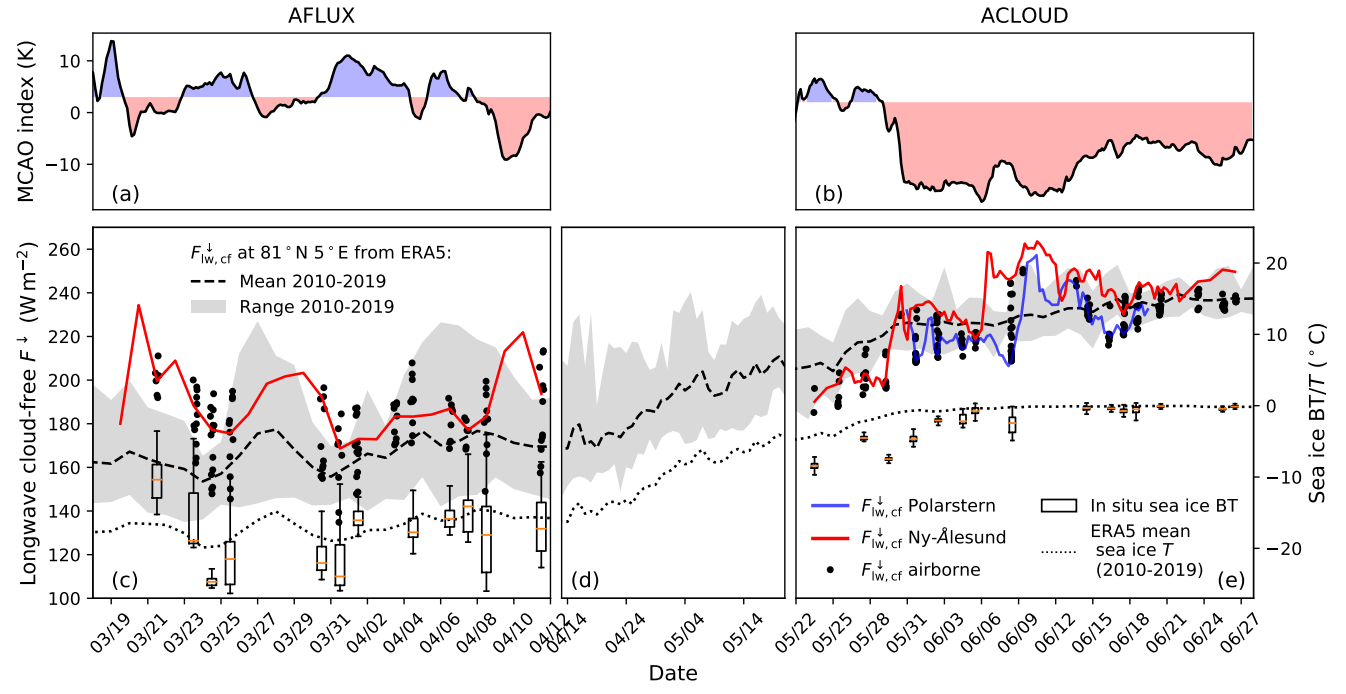

Figure 3. (a,b) Marine cold air outbreak (MCAO) index calculated from ERA5 reanalysis in the area between 77 and 80°N and 2.5 to 10°E, using a threshold of 3 K to characterize CAO dominated scenes (blue shading). (c-e) Time series of simulated cloud-free longwave downward irradiance from in situ profiles in the MIZ during AFLUX and ACLOUD (black scatter points), Ny-Ålesund, and Polarstern. 10 year climatological mean and maximum range from ERA5 reanalysis at (81°N, 5°E) is shown with black dashed lines and a grey shading. (c-e, right y-axis) Daily distribution of in situ brightness temperature (BT) above homogeneous sea ice (boxes as interquartile range, horizontal line as median, whiskers as range) observed during low-level flights and ERA5 10 year sea ice mean temperature.

a warm and a neutral period, during AFLUX, a more frequent shift between on-ice and off-ice flow pattern (positive MCAO index, bluish) occurred due to several low-pressures systems moving from the south of Greenland towards Svalbard. These events began with the advection of warmer air masses in the course of the low-pressure systems moving towards Svalbard, followed by strong northerly flows for several days induced by the low-pressure system located in the east of Svalbard.

With changing atmospheric temperatures and humidity, the longwave REB in the MIZ in the Fram Strait will be affected by these synoptic scale processes, which can be seen in the simulated cloud-free longwave downward irradiances ($F^{\downarrow}_{\mathrm{lw,cf}}$) (Fig. 3b). In the beginning of AFLUX a strong warm air advection caused a 40 W m^{-2} higher $F^{\downarrow}_{\mathrm{lw,cf}}$ compared to the ERA5 10 year climatological mean. With the beginning and intensification of a CAO period from 23 to 26 March 2019 the atmospheric temperatures as well as surface temperatures steadily decreased. The simulated in situ profiles in the MIZ (black scattered points) vary by up to 50 W m^{-2} distributed around the climatological mean above sea ice and increase towards the open ocean, illustrating the impact of the presence/absence of sea ice on the thermodynamics. Thereby, values frequently exceed the simulated $F^{\downarrow}_{\mathrm{lw,cf}}$ using radiosoundings from Ny-Ålesund, illustrating a warmer marine atmosphere compared to the local thermodynamic

https://doi.org/10.5194/acp-2021-279
Preprint. Discussion started: 26 April 2021


Atmospheric Chemistry and Physics Discussions

profiles embedded in the protected fjords of Svalbard. The sea ice surface brightness temperatures are distributed around the climatological mean and are clearly linked to the synoptic situation only in the beginning of the campaign. During the last two flights of the campaign, characterized by less dynamic conditions on large scales, a broad distribution of surface temperatures and $F^{\downarrow}_{\mathrm{lw,cf}}$ due to local thermodynamics (cloud-free and cloudy areas) were observed.

In the beginning of ACLOUD, the ERA5 climatology indicates an approximately $20\,\mathrm{W\,m^{-2}}$ higher $F^{\downarrow}_{\mathrm{lw,cf}}$ compared to the observed period of CAOs with colder atmospheric temperatures compared to the climatology. Due to weaker temperature gradients in the MIZ, the gradient of $F^{\downarrow}_{\mathrm{lw,cf}}$ decreased significantly compared to AFLUX. In the transition from the cold towards the warm period, the $F^{\downarrow}_{\mathrm{lw,cf}}$ increased by up to $30\,\mathrm{W\,m^{-2}}$ (mainly due to temperature advection in the free troposphere, Knudsen et al., 2018), while a second influx of warm and moist air (Knudsen et al., 2018) around the 10 June 2017 increased the $F^{\downarrow}_{\mathrm{lw,cf}}$ even more, underlining the importance of increased moisture in the advected air mass. The simulated in situ profiles transitioned between the $F^{\downarrow}_{\mathrm{lw,cf}}$ simulated using Polarstern radiosoundings (in the sea ice) and Ny-Ålesund emphasizing the areal variability in the region northwest of Svalbard.

In general, the conditions during AFLUX appear more synoptically driven compared to ACLOUD. Nevertheless, during both campaigns, the daily variability in cloud distributions and properties in the area clearly mask trends in the REB or CRF linked to synoptic processes (for example thermodynamic atmospheric background influence on CRF, Stapf et al., 2021) and underline that both aspects (synoptic scale and local effects) have to be analysed separately.

4 Radiative energy budget in the marginal sea ice zone

4.1 Seasonal two-mode structure of longwave net irradiances above homogeneous sea ice

As was illustrated in Section 3.2, the atmospheric thermodynamic structure over sea ice underlies a transition from a surface-based inversion-dominated, often also cloud-free, winter atmosphere towards a cloud-dominated boundary layer in summer. As the longwave net irradiances are basically a temperature difference between the effective radiative temperature of the atmosphere and the surface, seasonal characteristics and influences on the distribution of longwave net irradiances can be expected.

In Fig. 4, the longwave net irradiance distributions observed during SHEBA, N-ICE2015, ACLOUD, and AFLUX, are shown for certain periods to illustrate the transition from winter to summer. Similar to winter conditions observed during SHEBA and N-ICE2015 (Stramler et al., 2011; Graham et al., 2017), also during the ACLOUD/AFLUX campaign over closed sea ice (Ice Fraction $> 90\,\%$) mode structures appear in the frequency distribution of longwave net irradiances. However, the location of the individual modes during each season is shifted, and the difference between both increases towards the summer. The representative cloud-free mode is found, compared to winter (SHEBA, -40 $\mathrm{W\,m^{-2}}$), at around -60 $\mathrm{W\,m^{-2}}$ during late winter/early spring (AFLUX), and shifts even further to the negative during summer (ACLOUD, around -75 $\mathrm{W\,m^{-2}}$). The cloud-free mode during AFLUX indicates higher negative longwave net irradiances with low frequency of occurrence. This is less related to atmospheric fluctuations and rather the result of the heterogeneous surface temperatures (Fig. 2b), where for example snow-covered thin nilas or thinner ice floes appear to have significantly warmer surface temperatures compared to

https://doi.org/10.5194/acp-2021-279
Preprint. Discussion started: 26 April 2021

Atmospheric Chemistry and Physics Discussions

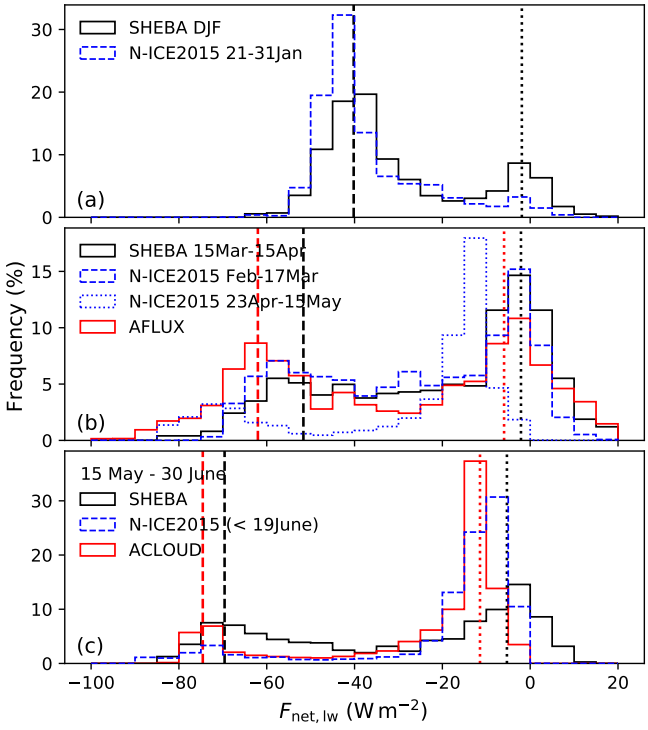

Figure 4. Histograms of longwave net irradiance observed during SHEBA, N-ICE2015, and AFLUX/ACLOUD ($I_f > 90$), for different time periods of the year (a-c). For SHEBA, AFLUX, and ACLOUD median values for cloudy (cloud fraction above 95 % or TWP (equivalent LWP) above 30 g m^{-2}, dotted vertical lines) and cloud-free (cloud fraction below 5 % or TWP (equivalent LWP) < 5 g m^{-2}, dashed vertical lines) conditions are given. No N-ICE2015 observations are available during the AFLUX period, and only a short, mainly cloud-free period in January. The ACLOUD distribution was weighted daily to reduce the impact of one extensive flight in cloud-free conditions.

thick sea ice. During ACLOUD with rather uniform temperature distributions of sea ice in the beginning melt season, those strongly negative values are not observed.

For the cloudy modes (distributed around zero), also a slight trend towards the summer to more negative longwave net irradiances in those opaque cloudy conditions is indicated. The median values decrease from SHEBA winter (-2 W m^{-2}) to AFLUX (-6 W m^{-2}) and ACLOUD (-11 W m^{-2}). Interestingly, the SHEBA longwave net irradiance distributions appear during all seasons slightly less negative, representing a weaker loss of energy in the longwave wavelength range at the surface in cloud-free as well as cloudy conditions. Especially during early summer, more neutral (distributed around 0 W m^{-2}) longwave net irradiances were observed along with a still frequent occurrence of positive values during SHEBA induced by a warmer cloud base compared to the surface. This state was not observed neither during N-ICE2015 nor ACLOUD and might represent a specific feature, potentially linked to the special near-surface thermodynamics or cloud properties of this region north of Svalbard.

https://doi.org/10.5194/acp-2021-279
Preprint. Discussion started: 26 April 2021


Atmospheric Chemistry and Physics Discussions

The parameters that control the individual modes are the surface temperatures in combination with the atmospheric thermodynamic profile that modifies, via stability/lapse rate and vertical profiles of absorber gases, the emissivity of the atmosphere or the effective cloud base temperature as a function of cloud base height and optical thickness.

With increasing temperatures from winter to summer and a large difference between atmospheric brightness and surface temperatures in cloud-free conditions, the non-linearity of the Planck radiation law is an important driver for the widening between both modes and the stronger loss of energy in the longwave wavelength range of the surface in summer. By assuming a theoretical combination of a surface temperature of -20 °C and a single layer 20 K colder cloud-free atmosphere a net longwave irradiance of -65 $\mathrm{W\,m^{-2}}$ would result, representative for early spring conditions. Scaling the same temperature difference (similar lapse rate) to a surface temperature of 0 °C in summer, results in a stronger loss of energy in the longwave range with -83 $\mathrm{W\,m^{-2}}$. In addition, the stability in cloud-free conditions degrades from winter to summer, which contributes to more negative longwave net irradiances in cloud-free conditions, where also the amount and vertical distribution of humidity plays an important role.

In cloudy conditions, a small difference between effective cloud-base and surface temperatures of, for example 2 K, results in -7 $\mathrm{W\,m^{-2}}$ and -9 $\mathrm{W\,m^{-2}}$ for the above mentioned simplified spring and summer surface temperatures, respectively. Thus, for the cloudy mode only a slight negative trend due to the Planck non-linearity towards summer can be explained. The major driver hereby might be the lapse rate between surface and cloud base controlling also the sign of longwave net irradiances, while for optically thinner clouds (below a saturated longwave CRF) also the strength of cloud top inversion still seems relevant.

During winter and early spring, in cloudy conditions (Fig. 2a, SHEBA winter and N-ICE2015 February and March) the lower atmosphere is often stably stratified. This constellation potentially enables a warmer cloud base temperature compared to the surface. The cloudy modes are relatively broad and distributed around zero during this period. The impact of synoptic systems in early spring reported by Cohen et al. (2017) as well as the thermodynamic diversity observed during AFLUX might explain the broadened cloudy and cloud-free modes, which were also observed during SHEBA, and might be typical for early spring.

With the shift to a cloud-dominated boundary layer in mid to late spring, the boundary layer becomes thicker and less stable, which supports colder cloud base temperatures relative to the surface depending on the cloud base height. For the conditions over sea ice during ACLOUD, clearly negative longwave net irradiances were observed due to a clearly separated cloud base from the surface and due to the absence of dense fog as during AFLUX. Especially, the thermodynamic profiles during N-ICE2015 (April/May Fig. 2b) illustrate the impact of the preconditioned less stable cloudy and cloud-free states that result in a more negative longwave net irradiance distribution (Fig. 4b, dotted blue).

The clear difference between the cloudy modes observed during ACLOUD and N-ICE2015 in early summer relative to SHEBA observations, seems to be less related to the average thermodynamic profiles shown in Fig. 2c, except that the SHEBA atmospheric profile is already slightly warmer. When the surface temperatures are fixed to zero degrees in the beginning melt season, further increasing atmospheric temperatures force a more stable near-surface layer or stronger temperature inversions, both might support more neutral/positive longwave net irradiances. Walden et al. (2017) (their Fig. 8) presented a mostly unstable near-surface layer during N-ICE2015 (2 m air minus surface skin temperature) in spring, similar to the conditions during

https://doi.org/10.5194/acp-2021-279
Preprint. Discussion started: 26 April 2021


Atmospheric Chemistry and Physics Discussions

ACLOUD (Fig. 2d). For the shown ACLOUD time period, SHEBA data indicate that the near-surface temperature difference was distributed around 0 K (distribution not shown), illustrating slightly more stable conditions, which might additionally contribute to the broader and more neutral cloudy longwave net irradiance mode.

Considering the modes as frequently preferred states of the longwave REB in the Arctic, the seasonal cycle of cloud fraction plays a crucial role. While during SHEBA winter, the cloud-free conditions outweighed the cloudy state (N-ICE2015 mostly cloud-free due to shorter period), early spring conditions seem to be more diverse, trending already slightly to a more frequent cloudy state. In early summer, N-ICE2015 and ACLOUD data indicate a dominant and less variable cloudy mode with only occasional and shorter cloud-free periods, while SHEBA data show a more divers character. With less frequent and probably shorter cloud-free periods in early summer, the thermodynamic adjustments of the cloud-free atmosphere might be less pronounced, resulting in weaker surface based inversions (N-ICE2015 April/May or May/June cloud-free profiles, Fig. 2), which would contribute to more negative longwave net irradiances in the cloud-free states.

The difference between cloudy and cloud-free modes can be understood as the climatological or measurement-based CRF (Stapf et al., 2021), defined by the average impact of the presence of clouds on the longwave REB. It can be estimated from the median longwave net irradiances of the modes in Fig 4 (dashed, dotted vertical lines). This difference increases from 39 $\mathrm{W\,m^{-2}}$ in winter (SHEBA) to 56 $\mathrm{W\,m^{-2}}$ in spring (AFLUX), and 63 $\mathrm{W\,m^{-2}}$ in summer (ACLOUD), illustrating the role of thermodynamics for the impact of clouds on the longwave REB. Even small changes of thermodynamic low-level structures, likely also synoptic scale circulation pattern, or regional characteristics, might be of relevance for those mode structures, or more general, the impact of the presence of clouds in the Arctic.

4.2 Longwave four-mode structures in the marginal sea ice zone

In contrast to the long-term ice floe camps as operated during SHEBA or N-ICE2015, the airborne observations during the ACLOUD/AFLUX campaign have been conducted in the heterogeneous MIZ. Therefore, the longwave net irradiances can be analyzed with respect to the surface type. In Fig. 5, the frequency distribution of longwave net irradiance is shown in a two-dimensional space spanned by the all-sky surface albedo and longwave net irradiance. This type of plot provides combined information on surface (sea ice concentration, albedo, and shortwave illumination conditions, cloudiness) and cloud conditions (cloud base height, optical thickness).

For both seasons, four maxima (modes) are obvious. For each surface type, ocean (depending on the SZA and illumination/cloudiness $\alpha < 0.1$ for ACLOUD, $\alpha < 0.2$ for AFLUX) and closed sea ice (depending on seasonal snow/ice property, $\alpha > 0.58$-0.75 for ACLOUD, $\alpha > 0.7$ for AFLUX), the cloudy (less negative) and cloud-free (more negative) modes are displaced (longwave net irradiance space). Therefore, instead of two modes over homogeneous sea ice, the MIZ is characterized by a four-mode structure.

Seasonal characteristics of surface and atmospheric properties during AFLUX and ACLOUD influence these mode structures. The most noticeable change between early spring (AFLUX) and summer (ACLOUD) is the gradient of the longwave net irradiance in the transition from ocean to sea ice. During spring (AFLUX), strong surface skin temperature gradients (up 25 K) were observed in the MIZ, while during the second half of ACLOUD (melt period) only up to 6 K were found due to an

https://doi.org/10.5194/acp-2021-279
Preprint. Discussion started: 26 April 2021

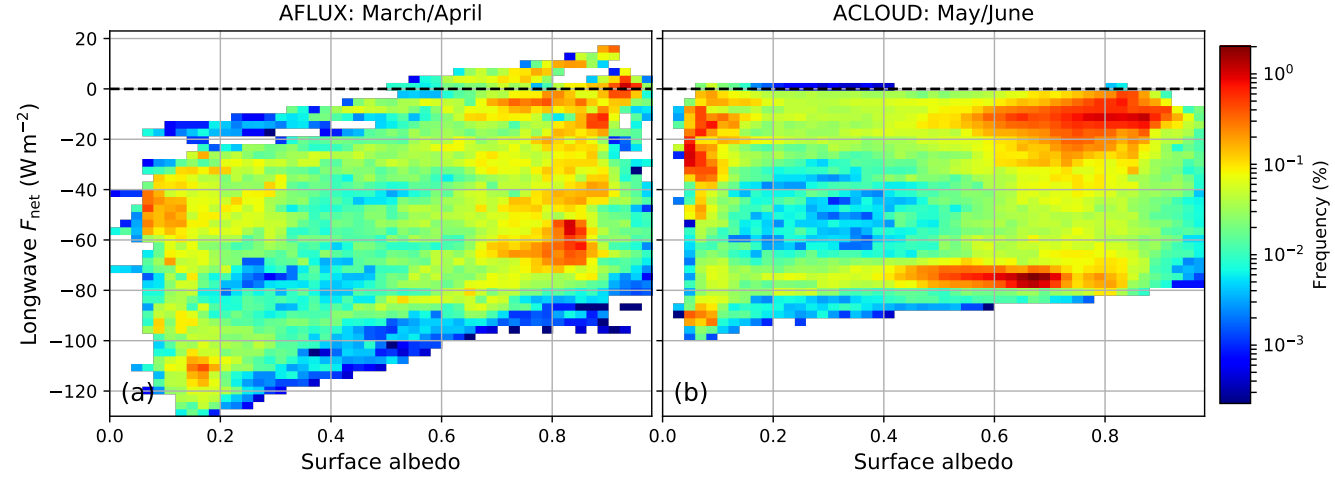

Figure 5. 2D histogram of longwave net irradiances as a function of all-sky surface albedo observed during AFLUX (a) and ACLOUD (b). The sea ice concentration increases with increases surface albedo. Modes on the right side represent sea ice conditions, modes on the left side the open ocean.

already warmer open ocean (leads excluded). However, it is important to note that a simple change in surface temperatures of the different surface types does not explain the change of longwave modes on larger horizontal scales. Scaling the average surface temperatures of the cloud-free mode during AFLUX above sea ice (-20.7 °C) and longwave net irradiances of -63 W m^{-2} to the observed ocean surface temperature (0.6 °C) would result in -151 W m^{-2}, while mostly only up to -120 W m^{-2} were observed in cloud-free conditions above sea ice. Consequently, the thermodynamic adjustment of the atmosphere in the MIZ towards open ocean as shown in Fig. 2b compensates on average up to 30 W m^{-2} in cloud-free conditions during AFLUX. Only on small scales, e.g. over sea ice with leads or nilas, the longwave net irradiances are shifted by the surface temperatures alone, since no rapid thermodynamic adjustment occurs there.

Especially the frequently observed off-ice flows (CAOs) during AFLUX strongly modify the REB in the MIZ and shift the longwave net irradiance modes by 50 W m^{-2} towards the ocean. During the ACLOUD campaign, with less dynamic conditions, the cloudy mode over open ocean shows two clusters, representing the still CAO-dominated May (distributed around -30 W m^{-2}, occasionally to -50 W m^{-2}) and the warm and neutral period of the campaign (Knudsen et al., 2018) distributed around -15 W m^{-2}.

Similar to the more variable mode structures in spring compared to early summer shown in Fig. 4, the appearance of the modes is more clearly distinguished and apparently more homogeneous during ACLOUD. Less variable surface temperature, thermodynamic profiles and a mostly cloudy boundary layer with radiative opaque clouds and similar cloud base heights compared to more variable and dynamic conditions during AFLUX represents clearly a difference between both seasons.

Due to the special characters of CAOs and warm air intrusions and their major impact on the REB, these synoptic scale processes are discussed in more detail in the following.

https://doi.org/10.5194/acp-2021-279
Preprint. Discussion started: 26 April 2021


Atmospheric Chemistry and Physics Discussions

4.3 Cold air outbreaks – off-ice flows

4.3.1 Surface radiative energy budget and impact of leads

During cold air outbreaks (CAOs) in the Fram Strait, the associated northerly flow advects cold and potentially dry inner Arctic air masses over the warm open ocean to the west of Svalbard. Extreme surface fluxes of heat and moisture in the unstable boundary layer over the open ocean cause strong convection and roll cloud formation in the evolving marine boundary layer (e.g., Brümmer, 1997; Pithan et al., 2018). Besides strong turbulent fluxes, also the longwave REB is shaped by these extreme conditions.

During AFLUX, a series of CAOs (23 to 25 March 2019, Fig. 3) was observed driven by a low-pressure system located east of Svalbard. Airmass trajectories from these three days (not shown) indicate that the air mass originated from further south, namely from the Norwegian and Barents Seas, advected around a low-pressure system located in the east of Svalbard. These trajectories likely explain the presence of some mid-layer clouds and even optical thick clouds over sea ice during the 24 March 2019. During a second period, starting end of March (Fig. 3), the air mass relevant for the 31 March 2019 originated from the inner Arctic without dense low-level clouds and only thin cirrus.

In Fig. 6a, the CAO observed during 25 March 2019 is illustrated together with the longwave net irradiances obtained during the low-level flight sections. Due to the absence of moisture sources over the cold, closed sea ice of the central Arctic and surface based inversion, one might expect cloud-free conditions over the sea ice region during CAOs. However, due to the presence of leads in the windward region and the resulting production of low, thin boundary layer clouds as well as advected mid-layer clouds (homogeneous cloud field westerly of the flight tracks), the conditions have been rather cloudy already above sea ice in the MIZ.

The presence of leads can influence the REB of the sea ice in the MIZ during CAOs by two processes. The first one is the production of thin, low clouds in the boundary layer evolving downstream of leads (Fig. 6a above sea ice) and the second one is a general warming and increase of the moisture content in the boundary layer.

Above sea ice, the observed longwave net irradiances fluctuate strongly between cloud-free scenes (-60 to -70 $\mathrm{W\,m^{-2}}$) and values up to -20 $\mathrm{W\,m^{-2}}$ below optically thick clouds. The thin and partly fog-like low clouds downstream of the leads produced a radiative transfer based longwave CRF of 10 to 30 $\mathrm{W\,m^{-2}}$. The simulated cloud-free downward irradiances (indicator for atmospheric temperature) shown in Fig. 6b increase for that day between the northern and southern east-west low-level section by 7 $\mathrm{W\,m^{-2}}$, while the southern section exhibits already a 5 K warmer surface (-20° C). Also during 31 March (no low-level clouds above sea ice), a steady increase of the simulated cloud-free downward longwave irradiance (Fig. 6b) of 10 $\mathrm{W\,m^{-2}}$ to 15 $\mathrm{W\,m^{-2}}$ towards a quite undefined, scattered ice edge is shown that illustrates the pure effects of the boundary layer warming of cold, inner-Arctic air masses in the MIZ. Thus, the local formation of leads in the MIZ is a relevant issue for the local REB and might contribute to the warming of the sea ice floe towards the open ocean even during CAOs.

As soon as the air mass reaches the warm ocean surface further downstream of the ice-edge, or in sea ice embedded leads or nilas, highly negative longwave net irradiances of up to -120 $\mathrm{W\,m^{-2}}$ (31 March 2019) were observed. Consequently, in addition to the strong turbulent fluxes in this region, radiative fluxes contribute to the strong surface cooling of the ocean in

https://doi.org/10.5194/acp-2021-279
Preprint. Discussion started: 26 April 2021

Atmospheric Chemistry and Physics Discussions

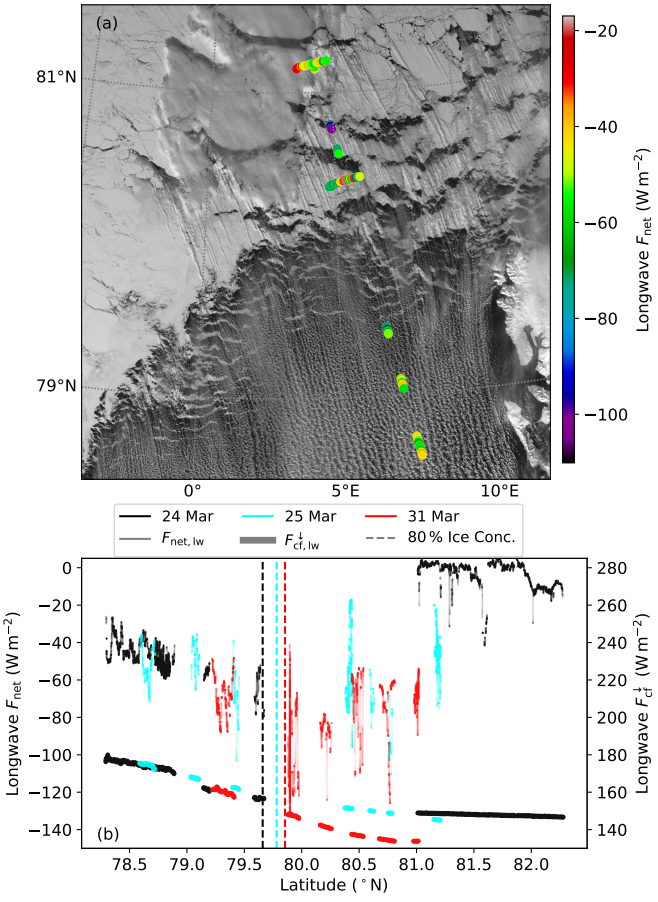

Figure 6. (a) Moderate Resolution Imaging Spectroradiometer (MODIS) satellite images of a CAO observed on 25 March 2019 overlaid by the observed longwave net irradiances during low-level flight sections. (b) Longwave net irradiances observed during the CAOs on 24, 25, and 31 March 2019 as a function of latitude. Simulated cloud-free downward irradiances are shown with thick lines. The latitude of satellite derived 80 % ice fraction (isoline) based on data from Spreen et al. (2008) is given with vertical dashed lines.

the absence of clouds (Fig. 6b, 31 March near the ice edge). Even in the presence of evolving roll clouds, strongly negative longwave net irradiances between -40 and -70 W m^{-2} were observed during AFLUX (Fig. 6b). Surprisingly, in the observed area, the strong change of surface temperatures (upward irradiances) is compensated by the evolving clouds resulting in a similar longwave surface REB over the partly cloud-free (optically thin clouds) closed sea ice and the cloudy open ocean. The average components of longwave REB and CRF (ΔF_{lw}) during four CAOs with suitable flight pattern are shown in Tab. 1 and illustrate this compensation. The thermodynamic profile adapts relatively slowly to the warmer ocean surface. Thereby, the longwave net irradiances increase continuously (Fig. 6b, e.g. 24 March 2019) with increasing distance from the ice edge, which is primarily caused by the temperature adaption of the boundary layer (simulated longwave downward irrradiance) and effective cloud base temperature to the new surface temperature.

https://doi.org/10.5194/acp-2021-279
Preprint. Discussion started: 26 April 2021

Atmospheric Chemistry and Physics Discussions

Table 1. Averaged components of longwave REB observed over sea ice ($I_f > 95\,\%$) and over open ocean ($I_f < 5\,\%$) for four CAOs (24, 25, 31 March, and 6 April 2019) during AFLUX. Over sea ice the values of the 24 March (advected extraordinary thick cloud layers) are excluded.

	$F_{\mathrm{net,lw}}$	$F^{\downarrow}_{\mathrm{lw,cf}}$	ΔF_{lw}	$F^{\uparrow}_{\mathrm{lw}}$
Sea Ice	-53.1	149.1	26.6	229.1
Open Ocean	-58.2	167.7	67.9	294.5
Difference	-5.1	18.6	41.3	65.4

The potential of CRF increases downstream, in addition to the increasing cloud optical thickness and cloud fraction, due to the transformation of the thermodynamic profile toward a negative lapse rate and weaker cloud top inversions. It is important to note that the temperature of the free troposphere often remains unchanged and mainly the evolving moist boundary layer is warming rapidly along the path southward (exemplary illustrated in Fig. A2a for the 23 March 2019). This results in a faster increase of the effective potential radiative cloud base temperature (boundary layer temperature) as observed during the 24 March 2019 (12 K, equivalent of 45 $\mathrm{W\,m^{-2}}$) compared to the cloud-free longwave downward irradiance increase of only 28 $\mathrm{W\,m^{-2}}$. During this flight (optically thick clouds already above sea ice) an increase of longwave CRF of 65 $\mathrm{W\,m^{-2}}$ to 80 $\mathrm{W\,m^{-2}}$ was observed.

4.3.2 Evolving boundary layer radiative energy budget

The unique feature of strongly negative longwave net irradiances during CAOs might become relevant also for the REB of the entire boundary layer, which partly converts the upward irradiance by absorption and re-emission. The components of boundary layer energy budget were quantified by Brümmer (1996, 1997) during multiple flights in CAO with in situ box pattern close to the surface and at the cloud top. In contrast to their approach, we quantify the contribution of radiative fluxes to the boundary layer REB using idealized radiative transfer simulations of thermodynamic profiles observed by the dropsondes released during AFLUX. We do so because the highly variable in situ radiation observations in the heterogeneous conditions during CAOs might be particularly error prone for this application. A further advantage of the usage of radiative transfer simulations is that it enables the analysis of continuous vertical profiles of longwave net irradiances and source and sink terms of the REB in the boundary layer column. This approach also allows the computation of potential radiative temperature change rates, which cannot be derived reliably from in situ observations due to the heterogeneous cloud structures in CAOs. The simulations and relevant features of radiative transfer in CAOs are introduced in the Appendix B and are shown for dropsonde observations of the 23 March 2019.

In Fig. 7, the simulated vertically integrated flux convergences and radiative temperature change rates for four CAOs (23, 24, 25, and 31 March 2019) based on suitable dropsonde observations (Appendix B) are shown. The series of dropsondes were released during a flight track roughly parallel to the direction of the mean boundary layer wind during the CAO. This enables

https://doi.org/10.5194/acp-2021-279
Preprint. Discussion started: 26 April 2021

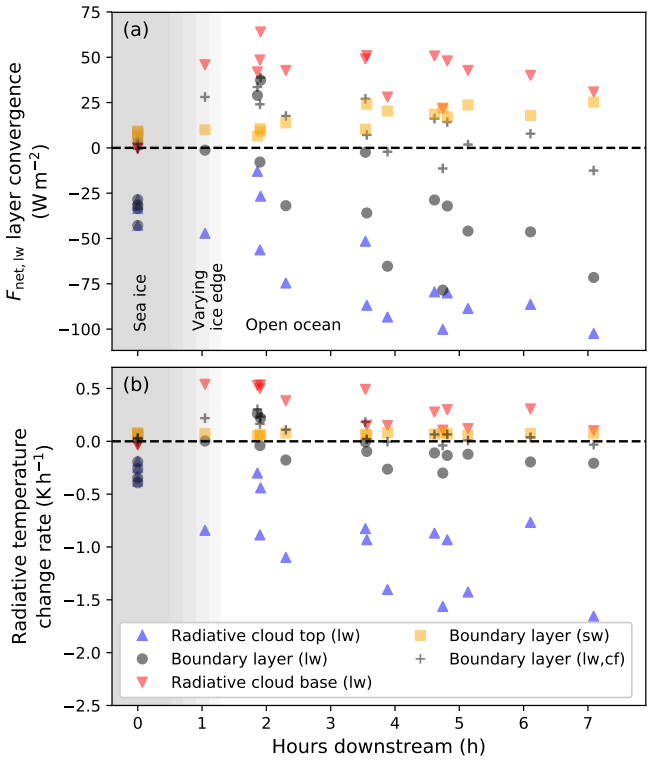

Figure 7. a) Net irradiance (longwave (lw), shortwave (sw, SZA of 70°) convergence (positive meaning absorbing) simulated from thermodynamic profiles (see Appendix B, Fig. A2) observed during 4 CAOs for the vertical layer of radiative cloud top and base (defined in Appendix B) as well the entire boundary layer (surface to cloud top inversion). b) Radiative longwave temperature change rates derived from the net irradiances in (a). Please note that both quantities are given for varying vertical layer thicknesses (legend) due to the evolution of the boundary layer (see Appendix B) and would normally be given in m^{-1}.

the calculation of the elapsed time in flow direction based on the observed horizontal wind speed and position similar to a trajectory and the quantification of radiative temperature change rates.

Over sea ice the presence of thin clouds induces a longwave net irradiance divergence between 28 and 43 $\mathrm{W\,m^{-2}}$ throughout the entire boundary layer, representing likely the major energy sink with radiative temperature changes of up to 0.4 $\mathrm{K\,h^{-1}}$ (entire boundary layer). As soon as those clouds reach the open water at the ice edge, the absorption of longwave irradiance in the cloud base will reach, or even exceed, the divergence at the cloud top depending on the individual cloud optical thickness and boundary layer height. The stronger the temperature gradient between air and sea surface temperature and the thicker the boundary layer (relatively cold cloud top), the stronger is the contribution to the boundary layer warming within the first 1 to 2 hours. In the frequently observed cloud-free area close to the ice edge (Gryschka et al., 2014) (before the development of roll clouds), the longwave irradiances will always contribute to a warming of the boundary layer as illustrated by the cloud-free simulations in Fig. 7 (up to 0.3 $\mathrm{K\,h^{-1}}$). With increasing distance from the ice edge, the absorption of longwave irradiance

https://doi.org/10.5194/acp-2021-279
Preprint. Discussion started: 26 April 2021


Atmospheric Chemistry and Physics Discussions

at the cloud base weakens due to the decreasing spread between surface and cloud base temperature. At the same time, the divergence at the radiative cloud top increases steadily up to 100 $\mathrm{W\,m^{-2}}$, so that this layer represents a strong sink of energy for the entire boundary layer. Consequently, with increasing distance from the ice edge a cooling of the entire boundary layer by the longwave irradiances will dominate. In case of an increasing cloud base height (spread between effective cloud base and surface temperature) the base warming and ocean surface cooling might increase again further downstream, which is not considered in the simulations as it was not observed during AFLUX.

The calculated radiative temperature change rates (Fig. 7b) need to be interpreted with caution. These values represent hypothetical temperature changes if no other fluxes (e.g., Brümmer, 1997) would contribute. Although the presence of a strong cloud top cooling is suggested, the actual temperature at the cloud top is increasing steadily in the observed area. The total boundary layer flux divergence tends to increase downstream, however, also the vertical extent of the boundary layer (mass of air) increases which counteracts the radiative temperature change rates. Nevertheless, this quantity gives an individual estimate of the contribution of radiative processes on the boundary layer warming observed during the first hours of CAOs.

On average, the longwave radiation cools the boundary layer along the trajectories with -0.06 to -0.22 $\mathrm{K\,h^{-1}}$ for the individual CAOs observed during AFLUX. Integrated, the longwave radiative temperature change rates compensate up 1.5 K (approximately 10 %) of the observed boundary layer warming within the first 7 hours. Later in the season, in late spring, the absorption of solar radiation (SZA of 70°, Fig. 7) has to be considered, which counteracts the longwave boundary layer cooling by up to 0.5 K within the presented time span.

The variety of thermodynamic profiles, inversion strengths, and absolute temperature gradients in the MIZ are crucial drivers of the longwave contribution to the boundary layer evolution and the transition of strong to weak cloud base warming in combination with a continuously increasing cloud top cooling might be of relevance for cloud structures evolving during CAOs.

4.4 Warm air intrusion – on-ice flow

During the ACLOUD and AFLUX campaigns, three cases of on-ice flows (21 March 2019, 8 April 2019, and 2 June 2017) were observed. In Fig. 8a-c the collocated MODIS satellite images are presented together with the longwave net irradiances during low-level flight sections. During 2 June 2017 (ACLOUD), a strong south-westerly on-ice flow caused by a high pressure system in the southwest of Svalbard advected optically thick clouds over the MIZ (Fig. 8a). Earlier in the season during AFLUX (8 April 2019), an on-ice flow characterized by weak wind and by fog occurring in the first few kilometers north of the ice edge (Fig. 8b) was probed. On 21 March 2019 a south-easterly advection of thick mid-level clouds due to a low-pressure system in the east of Greenland (Fig. 8c) has been observed. The three cases differ in the way the thermodynamic profiles (shown in Fig. 8g-i) transform along the on-ice flow and the altitude of the advected clouds. The effect of this evolution on the longwave REB in the MIZ is discussed in the following.

During 2 June 2017, a weak surface temperature gradient of 4 K between sea ice floes in the MIZ and the open ocean in the west of Svalbard might have been responsible for the height-independent temperature adaption below the cloud top inversion shown in Fig. 8g. This inversion was located around 750 m over the ocean and between 250 and 400 m in the MIZ, while

https://doi.org/10.5194/acp-2021-279
Preprint. Discussion started: 26 April 2021


Atmospheric Chemistry and Physics Discussions

the cloud top temperature remained almost constant. The observed longwave net irradiances during the low-level section (Fig. 8a) indicate that the cloud base temperature was consistently colder than the surface resulting in purely negative longwave net irradiance. Also, due to the absence of surface based fog, the surface still lost energy in the longwave wavelength range despite the advection of warm air. The observed longwave net irradiances over the ocean were slightly more negative (-10 $\mathrm{W\,m^{-2}}$ to -15 $\mathrm{W\,m^{-2}}$) due to a cloud base around 300-400 m. The first section above sea ice (optically thick and low clouds) shows a similar cloud base temperature as observed above the open ocean, but combined with a 2 K colder surface (-0.75° C), a longwave net irradiance around -5 $\mathrm{W\,m^{-2}}$ was observed. In the north, the broken and optically thinner clouds shifted the longwave net irradiances again to a range from -10 $\mathrm{W\,m^{-2}}$ to -15 $\mathrm{W\,m^{-2}}$ (occasional cloud openings more negative), while the surface temperatures were colder around -2° C. The observed warmer, and likely by the warm air advection already adapted, temperatures of the southern ice floes might explain the weakly negative longwave net irradiances. However, including the solar radiation (beginning of June, Fig. 8d), the shortwave cooling effect of clouds counteracts the longwave warming, although the surface albedo was still high. For the optically thicker part above sea ice (centered flight section), the net irradiances are less positive compared to the thin and broken clouds further north. In the north, the clouds are characterized by only a slightly weaker longwave warming effect, while in the shortwave range they exhibit a higher transmissivity that increases the surface net irradiances. Thus, surprisingly, a stronger surface warming (potentially higher surface temperatures) should be expected in the north rather than in the south over fractional sea ice cover.

For the weak on-ice flow on 8 April 2019 in Fig. 8b, a surface temperature spread of 25 K was observed between the open ocean and the cloud-free inner sea ice (-25° C). With a weak southerly flow, the warm and moist air was likely cooled and mixed over the ice floes causing condensation and the formation of a fog layer. At the top of this layer, strong radiative cloud top cooling induced the development of a cloud top inversion (Fig. 8h), likely further enhancing the condensation. Further north in the MIZ, the fog layer thinned out and the longwave net irradiance quickly reached strongly negative values around -60 $\mathrm{W\,m^{-2}}$, being typical for the presence of surface-based inversions in cloud-free conditions. The dense surface-based, low fog caused similar to conditions in clouds a neutral longwave net irradiance state by a temperature equilibrium between effective cloud base temperature (near-surface air temperature) and surface temperatures (observed by the KT19 radiometer), as the weak near-surface temperature inversion in cloudy conditions (temperature range between -16° C and -12° C in Fig. 8h) did not reach the surface. Radiative transfer simulations have been used to test the possibility of strongly positive longwave net irradiance, as airborne observation in 60 m to 70 m might be misleading. Only for a lifted fog layer, the longwave net irradiances were weakly positive and would have directly warmed the surface.

For the first two cases, a direct warming effect on the surface due to positive longwave net irradiances was not given. This was observed, however, during the 21 March 2019, where optically thick clouds in levels between 900 m and 1400 m were embedded in a warm air mass from a strong warm air intrusion event the day before (Fig. 8i, Fig. 3). During the low-level flight from east to west, the surface temperatures decreased from -8° C to -15° C and indicated along with the temperature profiles that the inversion was not necessarily surface-based, likely due to the heterogeneous sea ice observed during that flight or the radiative impact of the clouds on the surface. The potential cloud base temperature was found in the east and west at around -10° C. Consequently, as the surface temperature changed, the surface longwave net irradiance increased from east to west by

https://doi.org/10.5194/acp-2021-279
Preprint. Discussion started: 26 April 2021

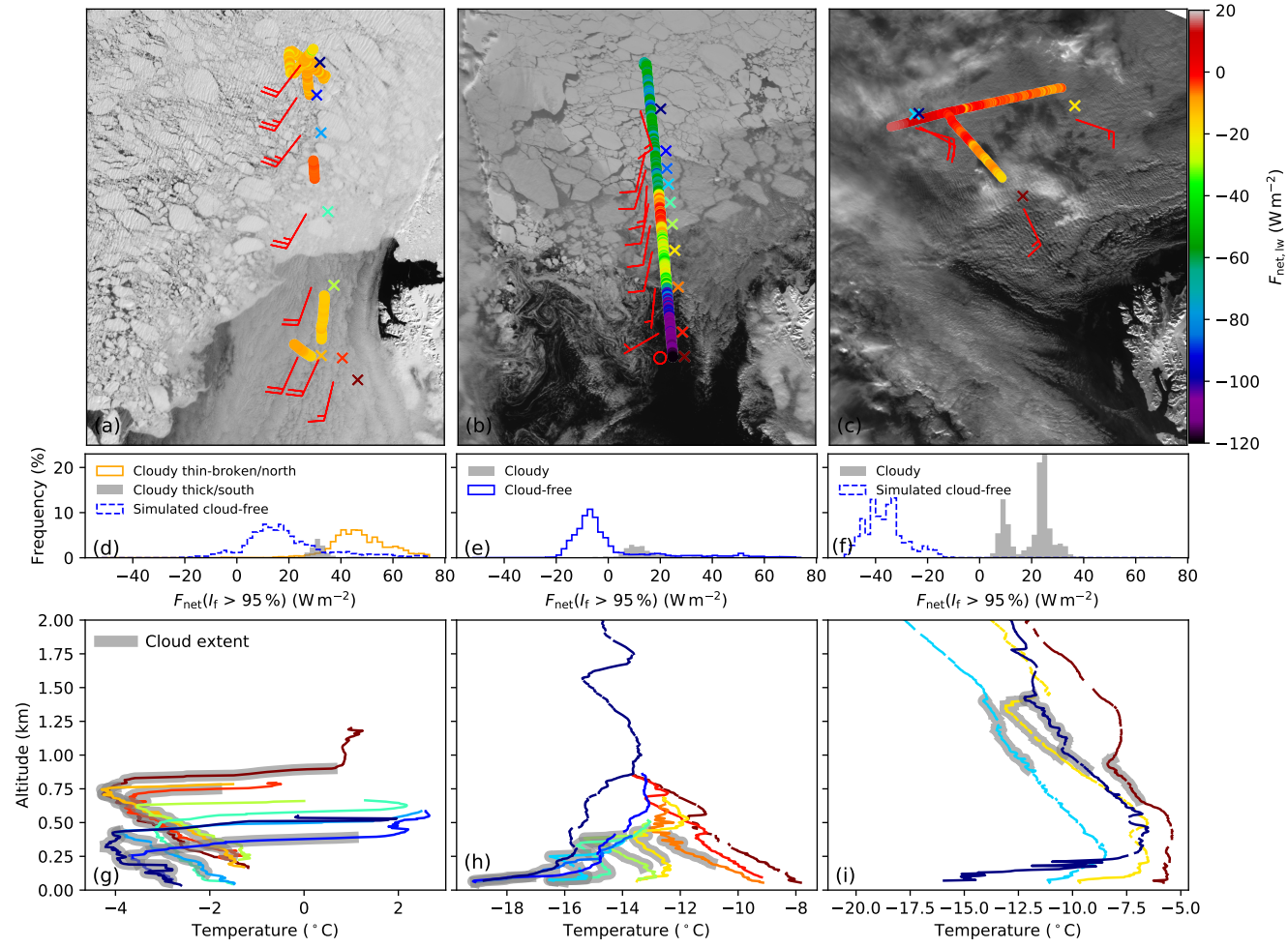

Figure 8. MODIS satellite images of three cases of on-ice flow during 2 June 2017 (a), 8 April 2019 (b) and 21 March 2019 (c) overlaid by longwave net irradiance during low-level flight sections. Location (offset for illustration) of in situ profiles of wind speed and direction (at cloud height), and temperature. (d-f) Shortwave plus longwave net irradiances of the low-level sections above homogeneous sea ice. (g-i) In situ temperature profiles colour-coded by the locations observed in panel (a-c). The cloud extent is illustrate with a grey shading.

almost 25 W m^{-2}, peaking in positive 17 W m^{-2} with a strong direct warming effect on the surface (surface gains energy). In the time series of surface brightness temperatures (Fig. 3), this event exhibits the warmest sea ice temperatures observed during AFLUX. After about an hour, due to an extensive stationary stair case pattern in the west, the light blue profile (Fig. 8i) was observed, illustrating the dynamic conditions during that flight. The atmospheric temperature decreased above the near-surface inversion by up to 3 K. Consequently, for the last low-level section towards southeast already a neutral lonwave net irradiance has been observed, steadily decreasing towards the ocean with warmer temperatures. Despite the weak solar insolation on this

https://doi.org/10.5194/acp-2021-279
Preprint. Discussion started: 26 April 2021


Atmospheric Chemistry and Physics Discussions

day, strongly positive total net irradiances (Fig. 8f) were observed towards the west, due to a decreasing cloud optical thickness enhancing the shortwave transmissivity.

The three cases underline the importance of thermodynamic profile transformation in combination with the cloud macrophysical and microphysical properties during on-ice flows, which directly controls the amount of energy absorbed by the sea ice in the MIZ. Lifted advection of clouds embedded in warmer air masses over colder sea ice and separated by a surface-based inversion, similar to the 21 March 2019, could produce an even stronger warming effect at the surface compared to near-surface fog (8 April 2019) due to higher potential effective cloud base temperatures. The presence of a surface-based inversion still likely contributes to a surface warming with turbulent heat fluxes. In case of cold, non-melting surface temperatures, a surface temperature response to the CRF is likely, shifting the longwave net irradiances back to negative values, including the heat fluxes. In the melt season this compensation/response is suppressed by the melting point of snow/ice, which might result in persistent warming/melting effects.

5 Cloud radiative forcing in the marginal sea ice zone

5.1 Sensitivity to sea ice concentration

In the MIZ, the areal averaged surface albedo is influenced by seasonal and microphysical snow and ice properties, but primarily it is controlled by the sea ice concentration. The albedo follows an approximately linear relation between the prevailing open ocean albedo and pure snow and ice albedo. As the cooling impact of clouds on the surface critically depends on the value of surface albedo, both sea ice concentration and snow microphysical properties control the CRF.

The total CRF obtained for both campaigns is presented together with the averaged satellite-derived sea ice concentration during ACLOUD (and AFLUX) in Fig. 9. It becomes clear that the variability of involved parameters makes the MIZ a truly complex region.

On larger scales the tendency of warming effects of clouds above sea ice and cooling effects above the ocean can be seen in Fig. 9. However, plenty of flight sections during both campaigns indicate a cooling effect also in sea ice dominated areas. On small scales mostly leads and dark nilas locally decrease the surface albedo and induce a negative CRF. For longer sections of negative CRF, the seasonal changes in SZA and surface albedo (beginning melt season during ACLOUD) are responsible, in addition to the synoptically driven cloud macrophysical and microphysical properties in the area. The distribution obtained from both campaigns underlines the complex and variable character of CRF when analysed over the heterogeneous sea ice conditions of the MIZ rather than in the context of long-term stationary observations.

To illustrate the role of ice fraction in the transition from a warming to a cooling effect of clouds in the MIZ, the CRF, accounting for the surface-albedo–cloud interaction, is shown in Fig. 10 as a function of the retrieved cloud-free albedo. In addition, mean values of observed CRF for certain ranges of ice fraction and SZA are shown, as well as radiative transfer simulated values using the averaged atmospheric profile and LWP during ACLOUD above sea ice (Fig. 1 and 2) as a reference. In the simulations, a snow grain size representative for fresh snow as observed during AFLUX and the beginning of ACLOUD is used with a specific surface area of $28\,\mathrm{m^2\,kg^{-1}}$ (snow grain size of $117\,\mu\mathrm{m}$) and an impurity load of $0.1\,\mathrm{ppmw}$. The simulated

https://doi.org/10.5194/acp-2021-279
Preprint. Discussion started: 26 April 2021

Atmospheric Chemistry and Physics Discussions

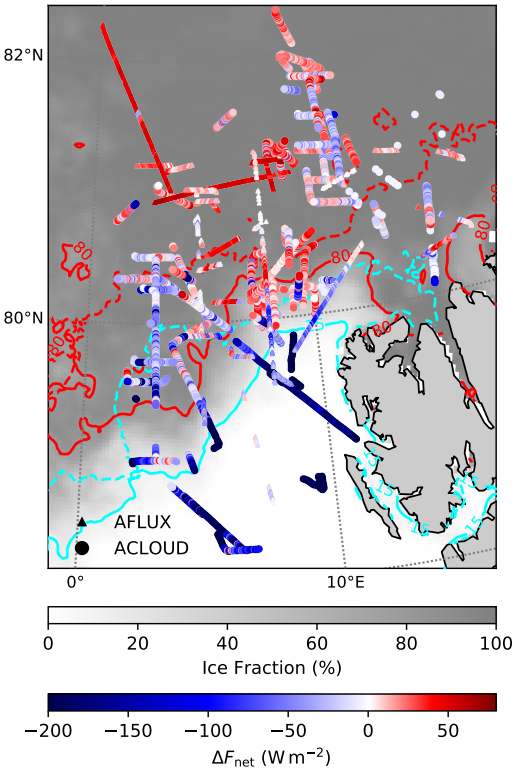

Figure 9. Distribution of total CRF obtained for the ACLOUD/AFLUX campaigns during cloudy scenes (LWP > 1 g m^{-2}). Campaign averaged satellite derived sea ice concentration (Spreen et al., 2008) of ACLOUD in the grey color scale. 80 % (red) and 15 % (light blue) isolines of I_f during ACLOUD (solid) and AFLUX (dashed). Values of total CRF can exceed the color scale.

cloud is located in a frequently observed vertical extent between 100 and 300 m and an average cloud droplet effective radius of 8 µm typical for this region (Mioche et al., 2017).

During early spring with weak solar insolation (SZA $< 80°$), clouds tend to warm the Arctic surface, regardless of the surface type. With decreasing SZA and constantly high snow albedo values in early spring, the sea ice concentration becomes the major surface parameter that controls the shortwave cooling potential of clouds. In comparison to the simulations, the observed mean CRF in the MIZ is mostly found in the lower range of ice fraction values of the simulations. This might be an indication that for fractional ice cover, the remaining ice floes might be less reflective than pure snow scaled as a function of sea ice concentration. A possible reason could be the presence of more new and thin ice in the vicinity of broken ice floes, which have a lower albedo relative to the ice-fraction–scaled snow of early spring conditions. For ACLOUD, also a stronger melt stage of the sea ice towards the open ocean might have reduce the albedo. In mid-June, even for homogeneous sea ice, the daily mean total CRF shifts toward a cooling effect due to the beginning melt season and the related decrease in surface albedo (Stapf et al., 2020). For high sea ice concentrations and fresh snow, the CRF values are clearly positive and are modified for

https://doi.org/10.5194/acp-2021-279
Preprint. Discussion started: 26 April 2021

Atmospheric Chemistry and Physics Discussions

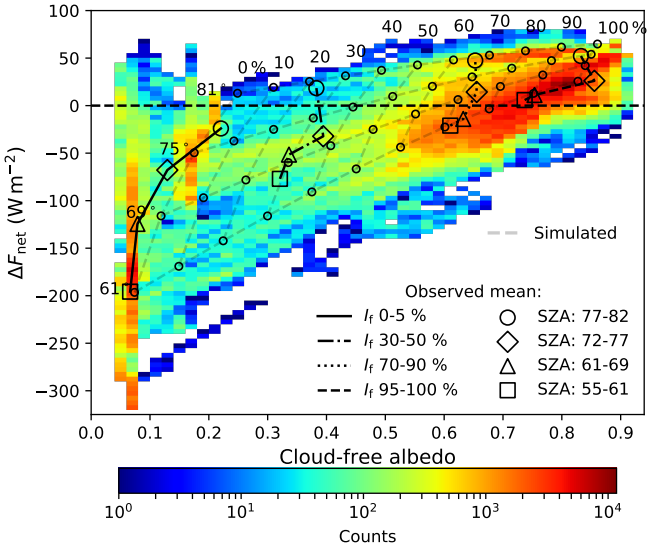

Figure 10. 2D histogram of total CRF during ACLOUD/AFLUX as a function of retrieved cloud-free surface albedo during cloudy scenes (LWP > 1 g m^{-2}). Overlayed scatter plot shows the mean total CRF/cloud-free albedo for certain SZA (scatter) and I_f (isolines) ranges. Thin dashed lines represent idealized simulations accounting for the surface-albedo–cloud interaction as a function of SZA (horizontal isolines) and ice fraction (vertical isolines) assuming a fixed cloud with a LWP of 50 g m^{-2} and snow specifications given in the text.

optical thick clouds above sea ice, like during ACLOUD, mainly due to the shortwave CRF (depending on SZA and LWP), as the longwave CRF is close to saturation.

Optically thinner clouds during AFLUX influenced also the difference between surface albedo in cloudy and cloud-free conditions (in addition to other parameters). On average, the albedo was 0.014 higher in cloudy conditions during AFLUX. As expected, this indicates a much weaker impact of the surface-albedo–cloud interaction compared to late spring early summer conditions during ACLOUD (Stapf et al., 2020), due to fresher and colder snow, optically thinner clouds, and higher SZA. For clouds with a equivalent LWP of below 10 to 15 g m^{-2} often also a higher cloud-free surface albedo was retrieved compared to cloudy conditions. This weakened the shortwave cooling effect of clouds, due to the strong shift between direct-dominated and diffuse surface albedo for high SZA. Nevertheless, on average, a 25 % stronger shortwave cooling effect (-16.8 instead of -13.4 W m^{-2} for a LWP > 1 g m^{-2}) was induced by the surface-albedo–cloud interaction during AFLUX, compared to a doubling of the shortwave CRF during ACLOUD (Stapf et al., 2020).

From spring to early summer, the ice fraction has to be considered together with the cloud optical thickness as the main parameter controlling the CRF as the snow surface albedo during this period shows only minor fluctuations. The radiative transfer simulated grid in Fig. 10 using fixed snow properties and LWP underlines these findings. However, the diversity of cloud conditions in this region prevents further conclusions or estimates of specific ice fraction values that represent the turning point from cooling to warming effects of clouds.

https://doi.org/10.5194/acp-2021-279
Preprint. Discussion started: 26 April 2021


Atmospheric Chemistry and Physics Discussions

Radiative transfer simulations further indicate that optically thick clouds above the open ocean in the presence of solar radiation are capable of compensating the radiative effect of a vanished sea ice only for an already low sea ice albedo in the beginning melt season. The increase of LWP which would be needed to maintain net irradiances during the transition from sea ice to the open ocean under these conditions depends on the SZA and the initial LWP above sea ice. Even the highest SZA of 55° would require an increase of more than $70\,\mathrm{g\,m^{-2}}$ of LWP. Insufficient statistics regarding cloud properties above the open ocean and sea ice limit further conclusions on this topic, but this compensation appears unlikely in the observed season and conditions (prior to the onset of melting sea ice) and might be more of relevance in the melt pond dominated season.

5.2 Sensitivity to cloud liquid water path

5.2.1 Longwave cloud radiative forcing

In theory, the longwave CRF of clouds is characterized by a strong non-linear dependence of CRF with increasing cloud optical thickness for optically thin clouds. In the MIZ, the LWP and the atmospheric thermodynamics change on small scales and the seasonal characteristics of atmospheric profiles were discussed in section 3.2. Both aspects might control the longwave CRF potential (convergence for high LWP) of clouds. In Fig. 11a the observed relation between LWP and radiative transfer based longwave CRF during AFLUX and ACLOUD in the MIZ northwest of Svalbard is shown as a 2D histogram together with the frequency distribution separated for both campaigns (Fig. 11b).

A strong increase of longwave CRF for an equivalent LWP below $25\,\mathrm{g\,m^{-2}}$ to values between 60 and $80\,\mathrm{W\,m^{-2}}$ illustrates the sensitivity of downward irradiance with respect to clouds. The importance of radiative opaque low-level clouds becomes obvious in Fig. 11b, where distinct modes for values above $50\,\mathrm{W\,m^{-2}}$ underline that the majority of cloud conditions in this region are represented by this cloud type characterized by a powerful longwave warming effect on the surface. During AFLUX (early spring), a higher frequency of intermediate longwave CRF values are caused by more diverse conditions, including optically thin, almost haze-like, low clouds or partly mid-layer clouds or even cirrus, which were less frequently observed during ACLOUD as single cloud layers. An increased ice water content of clouds during AFLUX likely contributed to a weaker longwave CRF for optically thin clouds.

For radiative-opaque conditions (LWP $>50\,\mathrm{g\,m^{-2}}$, $\Delta F_{\mathrm{lw}} > 50\,\mathrm{W\,m^{-2}}$), the modes of longwave CRF average $77\,\mathrm{W\,m^{-2}}$ for ACLOUD. As was shown in the seasonal longwave net irradiances mode structures over sea ice in Fig. 4, the climatological CRF (spread between cloudy and cloud-free modes), shows a distinct seasonal dependence due to thermodynamic specifications. Also the radiative transfer-based estimate for AFLUX (Fig. 11b blue) represents this feature with a reduced mean value for opaque low-level clouds of $71\,\mathrm{W\,m^{-2}}$. The difference between these two CRF modes (Fig. 11b) is consistent with the reported difference of the climatological CRF of $56\,\mathrm{W\,m^{-2}}$ during AFLUX, and $63\,\mathrm{W\,m^{-2}}$ during ACLOUD. Nevertheless, the presence of clouds appears to be less impactful on the longwave REB as estimated from the radiative-transfer based CRF, due to thermodynamic adjustments (Stapf et al., 2021).

To quantify the impact of thermodynamic profiles on the radiative transfer-based CRF, simulations of the average AFLUX and ACLOUD atmospheric thermodynamic profile (Fig. 2) are shown along with the observations in Fig. 11a. The simulated

https://doi.org/10.5194/acp-2021-279
Preprint. Discussion started: 26 April 2021

Atmospheric Chemistry and Physics Discussions

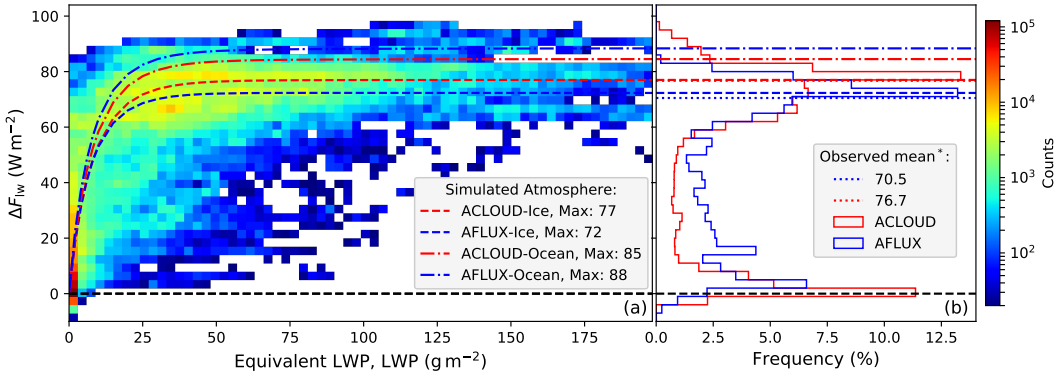

Figure 11. (a) 2d histogram of longwave CRF during ACLOUD/AFLUX as a function of retrieved LWP. Radiative transfer simulated values obtained from the averaged atmospheric profiles over the open ocean and sea ice during both campaigns (Fig. 2) and a cloud located between 100 m and 300 m are shown in dashed lines. (b) Frequency distribution of longwave CRF separated for both campaigns. Average observed saturated longwave CRF values (*: $\Delta F_{\mathrm{lw}} > 50\,\mathrm{W\,m^{-2}}$ and $\mathrm{LWP} > 50\,\mathrm{g\,m^{-2}}$) are given with horizontal lines.

longwave CRF (above sea ice) converges to similar values of 77 $\mathrm{W\,m^{-2}}$ during ACLOUD and 72 $\mathrm{W\,m^{-2}}$ during AFLUX, which is the direct cause of the less negative cloud-free reference net irradiances during AFLUX, induced by colder temperatures and a more pronounced temperature inversion above the boundary layer (Fig. 2). The impact of the lapse rate and temperature is even more powerful towards the open ocean as indicated by the simulations (Fig. 11a), which significantly increase the warming potential of clouds especially during AFLUX. While during ACLOUD regularly higher values of CRF around 80 to 90 $\mathrm{W\,m^{-2}}$ were observed, during AFLUX these values were surprisingly not observed. However, low-level flights with larger distance from the ice edge were limited during AFLUX, which might explain the lack of observed stronger longwave warming effects of clouds above the open ocean. During the CAO on 24 March 2019 (AFLUX), discussed in section 4.3.1, the longwave CRF steadily increased downstream of the ice edge and a further increase appears likely.

Besides the regional and more variable characteristics of CRF observed during AFLUX/ACLOUD in the MIZ, the longwave CRF values above sea ice are comparable to the ones reported for example in Ny-Ålesund (Ebell et al., 2020), where the longwave CRF converges to similar values of 75 $\mathrm{W\,m^{-2}}$. Sedlar et al. (2011) reported during August/September conditions further north of Svalbard (87°N) values between 70 and 80 $\mathrm{W\,m^{-2}}$ (often constant around 75 $\mathrm{W\,m^{-2}}$) with a similar thermodynamic profile as observed during ACLOUD. Interestingly, the distribution of longwave CRF in Ny-Ålesund (Ebell et al., 2020) appears to be more narrow considering a time period of two years (all seasons), which might represent a feature of the local atmospheric conditions. A more negative lapse rate reported in Ny-Ålesund compared to the inner Arctic, where the atmosphere is characterized by a more variable lapse-rate (as compared with N-ICE2015 by Kayser et al. (2017), or partly Knudsen et al. (2018) for ACLOUD/PASCAL) might be responsible for less variable longwave CRF as reported during SHEBA (Shupe and Intrieri, 2004) or observed in the MIZ. In general, the impression of a radiative transfer-based longwave CRF saturating

https://doi.org/10.5194/acp-2021-279
Preprint. Discussion started: 26 April 2021

Atmospheric Chemistry and Physics Discussions

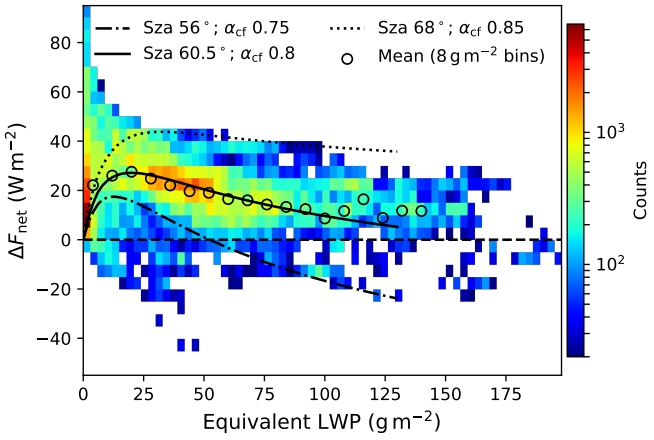

Figure 12. Total CRF as a function of the derived LWP during ACLOUD observed for scenes with a retrieved cloud-free surface albedo between 0.75 and 0.85 for the specific SZA accounting for the surface-albedo–cloud interaction. Simulated range of total CRF for the average ACLOUD atmosphere (Fig. 2) with a cloud between 100 m and 300 m and the observed SZA and surface albedo range during the campaign. Open circles show the averaged observations (8 g m^{-2} bins).

around 75 W m^{-2} appears to be a good estimate for the low boundary layer clouds frequently observed in this region from spring to autumn.

5.2.2 Total cloud radiative forcing

Combining the longwave and shortwave CRF in early spring (AFLUX), the total CRF above sea ice was positive throughout the campaign due to the high surface albedo and SZA. For these conditions, the total CRF is primarily controlled by the longwave CRF distribution (Fig. 11b), and thus, also the total CRF distribution appears similar. The opaque cloudy total CRF mode during AFLUX is shifted slightly from the distribution shown in Fig. 11b to around 50 W m^{-2} by the weak shortwave cooling effect. In late spring and early summer (ACLOUD), however, the shortwave cooling influence on the total CRF becomes more relevant.

In Fig. 12 the relation of observed total CRF and LWP during ACLOUD is illustrated for a selected range of retrieved cloud-free albedo values between 0.75 and 0.85. The simulated CRF of the averaged ACLOUD atmospheric profile and an assumed low-level cloud are show as a reference. The total CRF exceeds a tipping point for an increasing LWP, above which a significantly decreasing CRF is observed, potentially transitioning to a total cooling effect, depending on the SZA and surface albedo conditions.

The observations approximately peak in the LWP range between 15 g m^{-2} and 25 g m^{-2}, fluctuating between a total CRF of 20 g m^{-2} and 40 W m^{-2}. These values are representative for optically thin partly also broken cloud fields in low altitudes and have been frequently observed during ACLOUD. These clouds are known for a strong warming effect on the surface (Bennartz et al., 2013). More often however, clouds in the range between 30 to 55 g m^{-2} were observed for this surface albedo range.

https://doi.org/10.5194/acp-2021-279
Preprint. Discussion started: 26 April 2021


Atmospheric Chemistry and Physics Discussions

These clouds are characterized by a slightly weaker warming effect over sea ice and a more homogeneous character (less variable total CRF).

In general, the observed distribution follows the range described by the simulations, expect for low LWP. In this range, the total CRF frequently exceeds the theoretical weak CRF for those optically thin clouds. It should be noted that the LWP is derived by the shortwave transmissivity. Especially in the case of broken thin cloud conditions, the direct component of downward shortwave irradiance is partly not attenuated by clouds due to openings in the cloud field. In combinations with the still present diffuse shortwave irradiance by the surrounding clouds, the shortwave transmissivity suggests cloud-free conditions or even exceeds the value for cloud-free conditions due to the 3D effects. The longwave irradiance is mainly diffuse and thus even for small cloud openings in the cloud field high values of downward longwave irradiance are maintained. In combination, a stronger total warming effect of clouds can often be observed during these conditions compared to values expected by the 1D simulations. With increasing LWP of a cloud field, also the probability of openings decreases and these effects become less frequent. The total CRF values distributed below the simulated range can be attributed to conditions with a higher cloud base and a reduced longwave warming effect for a certain LWP value, which were rarely observed during ACLOUD.

If the 3D features are relevant for the areal-averaged surface REB with respect to simplified 1D radiative transfer and cloud-fraction assumptions, for example in regional climate models, or if they can be neglected on larger areas might be estimates by 3D radiative transfer studies similar to Benner et al. (2001), whereby the scale of heterogeneities and structures in the cloud field might be important for the non-linear increase of longwave CRF for optically thin clouds.

5.3 Total cloud radiative forcing and Arctic amplification above sea ice

As was shown in the previous sections, the radiative transfer simulations assuming a frequently observed low layer of Arctic boundary layer clouds represent the conditions during both campaigns fairly well and might be justified for this cloud type from spring to autumn in agreement with other studies in this region. Using these simulations, the tipping point of maximum total CRF (as shown in Fig. 12) was estimated for the observed atmospheric conditions in Fig. 13a depending on SZA, LWP, and cloud-free snow albedo for various grain sizes. This point also represents the pair of values of the highest total (solar plus longwave) net irradiances on sea ice (background of Fig. 13a).

Those tipping points are of great importance in order to assess whether future changes in LWP (cloud optical thickness), presumably forced by the Arctic amplification, will induce an increase or decrease of CRF and net irradiances over sea ice. These simulations hold for an increase of LWP in already cloudy conditions (typically high cloud fraction in summer), where the radiative transfer-based CRF can be used to estimate trends. In case of increasing cloud fractions, one might rather consider a observation-based CRF approach (analysis of longwave modes structures) to quantify the impact of the increasing presence of clouds based on the observed REB climatology (Stapf et al., 2021).

Starting from the cloud/surface regime (pair of values; seasonal SZA, albedo, LWP), such as observed during AFLUX/ACLOUD, optically thin clouds and high surface albedo values in spring (AFLUX), are prone to be sensitive to an increase of LWP (trend) due to the dominant and sensitive longwave CRF for this cloud/surface regime. On the other side of the tipping point and later in the season, as observed during ACLOUD, clouds are optically too thick to produce positive trends in net irradiances, further

https://doi.org/10.5194/acp-2021-279
Preprint. Discussion started: 26 April 2021

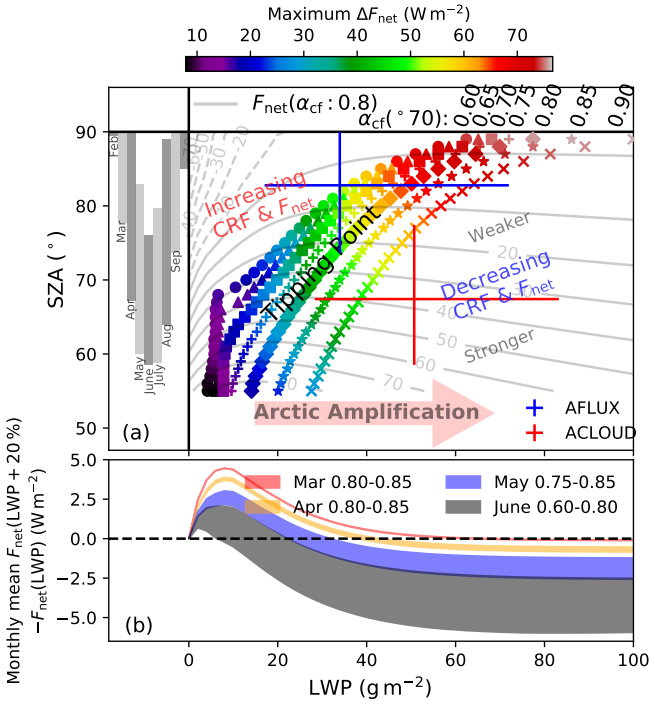

Figure 13. (a) Simulated pair of values of SZA and LWP for the maximum total CRF (colored scatter points) expected for the average ACLOUD atmospheric profile and a low-level cloud. The simulations are performed for different surface snow types (grain size) accounting for the surface-albedo–cloud interaction. The snow grain size dependent α_{cf} is given for a SZA of 70°. Net irradiances for surface albedo type $\alpha_{cf}(70^\circ) = 0.8$ are shown in the background as contour lines. In the left, SZA ranges at 82°N are given. Interquartile range of LWP observed during ACLOUD/AFLUX and SZA range expected during this season (crosses). (b) Potential change in monthly mean net irradiances assuming an increasing LWP of 20 % assuming a common albedo/snow grain size range (reference value for SZA of 70°) from spring to early summer. Lower line corresponds to lower surface albedo values.

supported by a decreasing surface albedo towards melt conditions that further enhance the cooling potential of clouds at the surface.

Although the likely sign of net irradiance changes is governed by the season (positive during the longwave-dominated winter, mostly negative during the shortwave-dominated summer) the absolute values as well the trends depend on small shifts in albedo and cloud optical thickness, especially during the transition in spring and autumn. In Fig. 12 and the background of 13a, the slope and absolute change in CRF and net irradiances is highly variable depending on the combination of SZA (season), LWP, and surface albedo.

Therefore in Fig. 13b, a hypothetical increase of LWP by 20 % from an initial LWP was used to demonstrate expected changes in monthly averaged net irradiances depending on the season and snow grain size. Especially in the range between 20 and 50 g m^{-2}, even small deviations of the initial LWP of 10 g m^{-2} may result in a significantly different expected trend of the

https://doi.org/10.5194/acp-2021-279
Preprint. Discussion started: 26 April 2021


Atmospheric Chemistry and Physics Discussions

surface REB. It should be mentioned that not only the absolute values of net irradiances and CRF depend the snow grain size, but also the expected trend in net irradiances (e.g. May). This relation clearly illustrates that potential changes in net irradiances in the future Arctic will depend on a delicate representation/estimate of cloud optical thickness and sea ice properties.

6 Summary and conclusion

We have presented REB and CRF observations in the heterogeneous environment of the MIZ northwest of Svalbard in spring and early summer. The REB in this region is driven by the sea ice concentration and the thermodynamic transition between the relatively warm ocean and the cold sea ice. Small-scale fluctuations of surface properties and thermodynamic profiles make this region a complex terrain for radiative processes. Several characteristic features have been observed during AFLUX and ACLOUD.

The longwave net irradiance two mode structure (above sea ice) is subject to a seasonal shift toward more negative irradiances in both modes and a more frequent cloudy state towards the summer. The individual distribution of a state is likely linked to seasonal thermodynamic profile characteristics, which control the distribution of cloud-free and cloudy net irradiances. Compared to SHEBA, the distributions north of Svalbard during spring and summer obtained from N-ICE2015, AFLUX, and ACLOUD, indicate a shift toward the negative in both states, likely due to less stable near-surface atmospheric conditions in this region.

For both surface types in the MIZ (open ocean, sea ice), two separated modes of longwave net irradiance are observed. On small horizontal scales in the MIZ they are induced by the obvious change of surface temperature between sea ice and leads/nilas. On larger horizontal scales the adjustment of the atmospheric thermodynamics and cloud properties relocate the longwave modes over the open ocean. Strongly negative longwave net irradiances in cloudy as well as cloud-free conditions represent a special feature in the MIZ due to the large spread between air/atmospheric and surface temperatures, especially during CAOs.

In the evolving boundary layer of CAOs, the longwave radiation represents a sink of energy, counteracting the strong sensible and latent heat fluxes that warm the boundary layer. Our simulations indicate that only for an area close to the ice edge, in the presence of particularly strong temperature gradients, a short-term warming contribution due to longwave radiation to the boundary layer warming of up to 40 $\mathrm{W\,m^{-2}}$ can be expected. This contribution transforms into a cooling of the boundary layer by up to -75 $\mathrm{W\,m^{-2}}$ further downstream, depending on the individual cloud and thermodynamic evolution.

The presence of leads/nilas upstream of the ice edge induces enhanced downward longwave irradiances via cloud production and boundary layer warming/moistening during CAOs and thus likely contributes to a warming of the ice floes in the MIZ.

The impact of warm air intrusions on the local sea ice REB in the MIZ is sensitive to the thermodynamic profiles along the flow and the vertical location of clouds. We observed that the strongest direct warming potential of clouds in the longwave wavelength range is found for an advection of clouds aloft embedded in the warm air masses, rather than fog embedded directly in strong surface based temperature inversions, and not necessarily for the optically thickest clouds in the presence of solar irradiance.

https://doi.org/10.5194/acp-2021-279
Preprint. Discussion started: 26 April 2021


Atmospheric Chemistry and Physics Discussions

In spring and early summer with a relatively constant and high surface albedo of sea ice, the sea ice concentration is the primary parameter controlling the total CRF in the MIZ.

The low altitude of the observed clouds (especially during ACLOUD) enabled the reproduction of longwave CRF by simplified radiative transfer simulations. The results indicated a seasonal dependence of maximum longwave CRF (increasing towards summer) driven by atmospheric thermodynamic characteristics. In comparison to other studies in the area around Svalbard, values of around 75 $\mathrm{W\,m^{-2}}$ seem to be typical.

The maximum total CRF was found for optically thin and partly also broken low-level clouds (3D effects of combined diffuse longwave and direct shortwave irradiance), whereby a delicate function of LWP and sea ice albedo controls the tipping point, from which a further increase of cloud optical thickness will result in lower net irradiances and weaker total CRF, as often observed during ACLOUD.

The MIZ represents a complex environment regarding radiative transfer and thermodynamic processes. Aside from representing only a small area of the Arctic, understanding and modelling the processes in this area is a challenge, but also an opportunity to improve the understanding of the REB in the inner Arctic. The extreme changes of boundary layer thermodynamics and its impact on the longwave REB in the MIZ, likely overdraw the importance of the thermodynamics. However, even slight shifts in the longwave net irradiance modes structures above homogeneous sea ice underline the importance of the linkage between low-level atmospheric profiles and stability, in cloudy as well as cloud-free conditions.

The agreement between radiative transfer simulations of simplified low-level clouds and averaged thermodynamic profiles, is encouraging, because improvements in the representation of the boundary layer thermodynamic profile in climate models might enable a powerful improvement of the surface REB during that season.

The delicate tipping point of total CRF and surface net irradiances, however, underlines the requirements of a precise representation of the cloud/surface regime in the specific season, as the impact of changing cloud fraction and optical properties in a future Arctic depends on a complex interaction of microphysical snow and ice properties and, precisely, these cloud properties. The sign of cloud feedbacks depends on the cloud/surface regime in the individual models, which will likely vary on regional, seasonal scale, or in terms of the observed Arctic amplification on the real character of the rarely observed low-level clouds in the Arctic. "Inserting" specific cloud and surface regimes, either from climate models, or observed from an increasing number of datasets in the inner Arctic (e.g., Achtert et al., 2020), in individual radiative lookup tables, might give some evidence in expected trends.

Being in the right regime of cloud and surface properties is a challenge for climate models. Considering insufficient statistics on real cloud properties over the entire inner Arctic, as well as diverging/variable estimates from satellite, models, and observations (Zygmuntowska et al., 2012; Cesana et al., 2012; Pithan et al., 2014; Achtert et al., 2020), conclusions on potential future cloud impact in the Arctic appear challenging.

Data availability. The combined ACLOUD and AFLUX low-level dataset (REB, CRF) is made (currently) available on the PANGAEA database. The ACLOUD broadband irradiance dataset is available in Stapf et al. (2019) and is made (currently) available for AFLUX

https://doi.org/10.5194/acp-2021-279
Preprint. Discussion started: 26 April 2021

Atmospheric Chemistry and Physics Discussions

on PANGAEA. Broadband radiation data and radiosounding data of the N-ICE2015 campaign are used from Hudson et al. (2016) and Hudson et al. (2017), for SHEBA from Persson (2011) and Moritz (2017). The ERA5 reanalysis Hersbach et al. (2018a) and Hersbach et al. (2018b) have been obtained from Copernicus Climate Change Service (C3S) Climate Data Store (CDS) (https://cds.climate.copernicus.eu). Air temperature, relative humidity, and pressure in situ profiles from both aircraft are used from (Hartmann et al., 2019), dropsondes from Ehrlich et al. (2019a) and Becker et al. (2020). The radiosoundings from Ny-Ålesund are available from (Maturilli, 2020) and for Polarstern from (Schmithüsen, 2017).

Appendix A: Surface-albedo–cloud interaction over open ocean

Similar to sea ice and snow surfaces, the illumination conditions, controlled by the solar zenith angle, atmospheric scattering, and the presence of clouds, modify the reflection properties of the open ocean. In Fig. A1a the surface albedo of the ocean is shown as a function of SZA using the direct fraction simulated for the average ACLOUD atmospheric profile. With increasing SZA (range representative for the Arctic), also the ocean albedo increases. For SZA above 85°, the fraction of direct irradiance (dashed line) decreases drastically, which causes an decrease of surface albedo towards 90°. For SZA above 70°, the wind speed becomes a crucial parameter for the ocean albedo and can induce changes by almost 0.2 for the given wind range. Relevant for the derivation of CRF above the ocean is the change between diffuse (dotted line in Fig. A1a) and the albedo in theoretical cloud-free conditions (dominated by direct radiation). Similarly, the CRF estimates using the observed ocean albedo in cloudy conditions (dotted line, values around 0.06) or the respective one in cloud-free conditions are shown as a function of SZA in Fig. A1b. These results hold for sufficiently optically thick clouds to induce a purely diffuse surface illumination, whereby the diffuse albedo remains constant with increasing LWP.

For high SZA the neglect of surface-albedo–cloud interactions above open ocean causes an overestimate of the shortwave cooling effect of clouds. Values can reach up to almost $40\,\mathrm{W\,m^{-2}}$ in calm wind conditions, which represents relative errors beyond 70 % (for LWP of $50\,\mathrm{g\,m^{-2}}$ and SZA above 80°). Wind speed induced fluctuations in ocean albedo modify the estimated CRF by up to 40 %. Especially during CAOs in early spring with strong wind periods the cooling potential of clouds will be enhanced while for weak wind areas or leads embedded in sea ice the cooling effect will be weaker.

An additional source of uncertainties represents the background aerosol, which can not be measured in case of cloudy conditions. An increasing AOD will reduce the fraction of direct irradiance and consequently manipulate the cloud-free ocean albedo required for the estimate of CRF. Looking at the potential uncertainties especially for SZA above 80° the derivation of CRF becomes challenging and uncertainties in the radiative transfer simulations become critical. Additional uncertainties remain due to the impact of reduced fetch in sea ice leads, which might reduce the surface roughness and whitecaps for a certain wind speed compared to the open ocean and might induce a slight overestimate of shortwave cooling effect in these situations.

https://doi.org/10.5194/acp-2021-279
Preprint. Discussion started: 26 April 2021

Atmospheric Chemistry and Physics Discussions

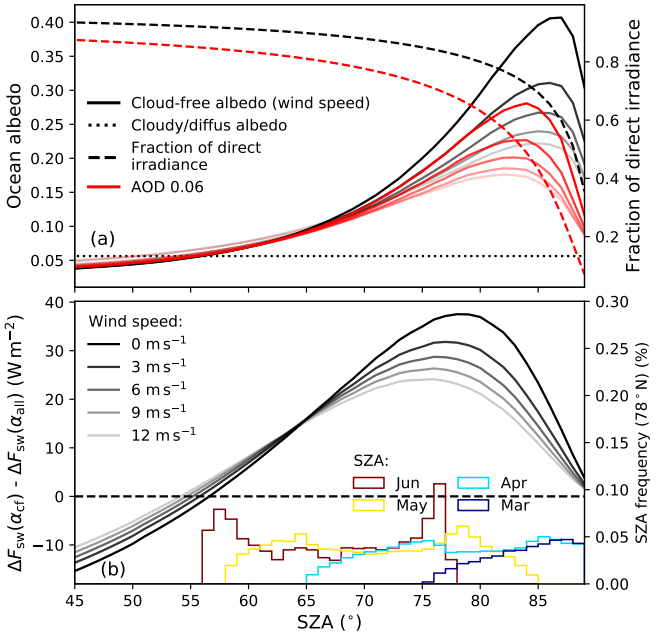

Figure A1. a) Ocean albedo in cloud-free and cloudy conditions after the parameterization of Jin et al. (2011) for various wind speeds and as a function of SZA. Impact of wind speed on diffuse albedo (< 0.003) is neglected. Second x-axis shows the fraction of direct to global irradiance for the average ACLOUD atmospheric profile. Red lines represents both quantities for an atmospheric aerosol optical thickness (AOD) of 0.06. b) Difference of shortwave CRF derived using the ocean albedo in cloud-free conditions for various wind speeds and the observed one in cloudy conditions. Histograms of monthly SZA at 80°N are shown in the second y-axis as a reference.

Appendix B: Estimate of radiative flux convergence/divergence during cold air outbreaks

To estimate the absolute contribution of radiative (diabatic) processes to the temperature changes of the boundary layer during CAOs, radiative transfer simulations of thermodynamic profiles obtained from dropsondes were used. The temperature profiles for a CAO on 23 March 2019 (AFLUX) are shown as an example in Fig. A2a. In the simulations, the clouds have been assumed to be surface-based (frequently observed during AFLUX CAOs) with a sub-adiabatic liquid water content (LWC) profile (constant fraction $f_{\mathrm{ad}} = 0.5$ of the adiabatic value) with a cloud droplet effective radius of 8 µm. The inversion base is assumed to be the level of the cloud top. The northern most profile (coldest boundary layer) was recorded over the sea ice covered area (assumed surface albedo 0.8), while the following dropsondes were ejected above the open ocean, whereby a simplified, constant surface skin temperature of zero degrees was assumed.

For the sea ice profile, the simulated profiles of longwave net irradiance (Fig. A2b) indicate a flux divergence (radiative cloud top cooling) throughout the whole boundary layer due to the optically thin cloud. As soon as these cold and thin clouds are advected above the sea ice edge (located between the two northernmost profiles) the surface temperature changes by almost 20 K and induce strongly outgoing longwave net irradiances of in this case up to -72 W m^{-2} even in cloudy conditions. With

https://doi.org/10.5194/acp-2021-279
Preprint. Discussion started: 26 April 2021

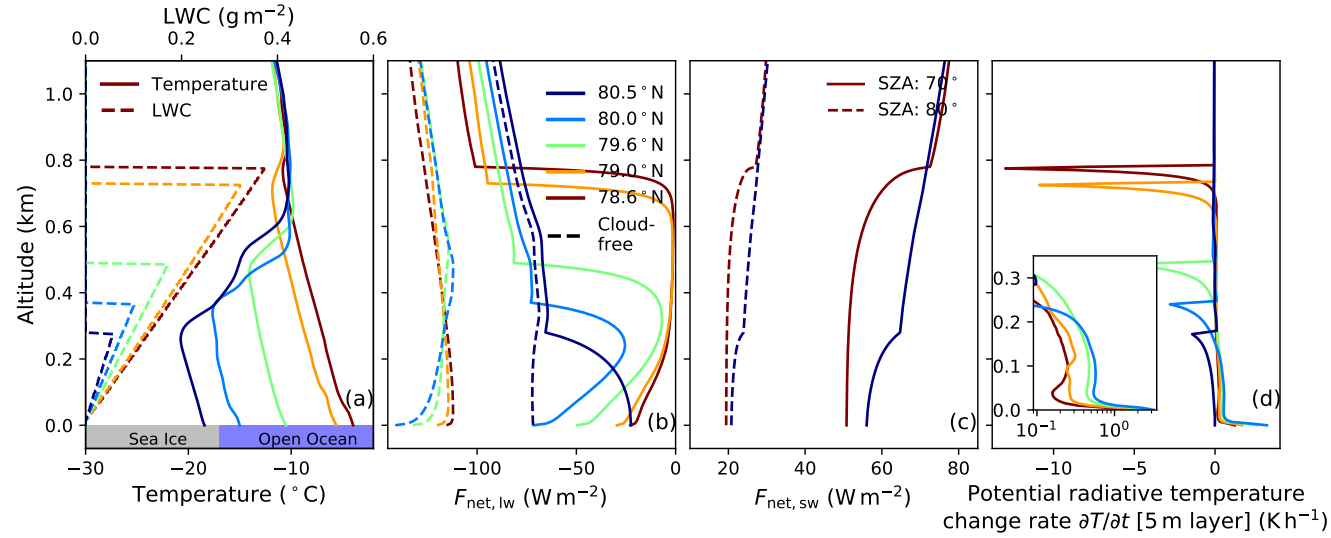

Figure A2. a) Temperature profiles derived from dropsondes during the CAO observed on 23 March 2019 at a latitude indicated by the legend and calculated sub-adiabatic LWC ($f_{\mathrm{ad}} = 0.5$). Radiative transfer simulated longwave ($F_{\mathrm{net,lw}} = F^{\downarrow} - F^{\uparrow}$, negative meaning surface loses energy) (b) and shortwave net irradiances (c), and theoretically expected (potential) radiative temperature change rates (shortwave (SZA of 70°) plus longwave) (d).

the increasing optical thickness of the clouds, a part of the upward irradiance is absorbed in the cloud base (radiative cloud base warming) indicated by increasing longwave net irradiances, until at a specific altitude, the highest net irradiances are observed. From this level, the relatively warm cloud emits radiation towards the cold upper atmosphere inducing the cloud top cooling (radiative cloud top, decreasing longwave net irradiances). The diabatic temperature change rates (potentially) caused by the absorption or emission of radiation in a certain atmospheric layer:

$$\frac{\partial T}{\partial t} = \frac{1}{\rho \cdot c_{\mathrm{p}}} \cdot \frac{\partial F_{\mathrm{net}}}{\partial z}, \tag{B1}$$

with the air density ρ and specific heat c_{p} are shown in Fig. A2d. With increasing LWC, the net irradiance in the cloud will saturate close to zero and will reduce the vertical extent of the radiative cloud top. This enhances the potential temperature change rate but not the integrated flux divergence. The cloud top cooling potential during CAOs increases with increasing distance from the ice edge. This is caused by a sufficiently high LWC inside the cloud layer causing maximum (neutral) longwave net irradiances inside the cloud (Fig. A2b) and, more importantly, by a decreasing temperature spread between the cloud top and the upper atmosphere (Fig. A2a). A relatively warm cloud top inversion results in a higher downward irradiance at the cloud top, which results, together with a colder cloud top temperature, in an weakly negative longwave net irradiance at the cloud top, commonly found over the sea ice or close to the ice edge. With the temperature adaption of the boundary layer to the new environment, also the temperature spread at the cloud top decreases, resulting in consistently increasing negative

https://doi.org/10.5194/acp-2021-279
Preprint. Discussion started: 26 April 2021


Atmospheric Chemistry and Physics Discussions

longwave net irradiances and divergence in the radiative cloud top downstream supported also by the non-linearity of the Plank radiation law.

For the radiative cloud base, the temperature adaption of the boundary layer reduces the spread between surface and air temperature and consequently the surface longwave net irradiances become less negative (observations in Fig. 6b) and the flux convergence at the cloud base downstream decreases.

The total boundary layer (surface to cloud top) flux divergence in this particular case is always negative (cooling the entire boundary layer). Only the first profile above the ocean shows the same amount of gain and loss of energy. In case of a strong air-surface temperature contrast in this area, also a gain of energy in the entire boundary layer is possible due to more negative net irradiances in the cloudy state which depends on the individual strength of the CAO. For cloud-free conditions close to the ice edge (dashed profiles Fig. A2b) the boundary layer will gain energy. Also in hypothetical conditions without roll cloud formation the boundary layer strongly absorbs the upward irradiances, shifting towards a weak cooling downstream with increasing distance from the ice edge.

The shortwave convergence of fluxes is shown for two SZA in Fig. A2c and is in general weak and might only be relevant in late spring, where it has to be consider as a compensation of the flux divergence of the whole boundary layer in the longwave range.

Vertically integrated flux divergences and potential radiative temperature change rates are discussed in Fig. 7 for four different CAO observed during AFLUX with suitable flight pattern and dropsonde releases.

Author contributions. All authors contributed to the editing of the article and to the discussion of the results. JS processed the radiation data, merged the datasets, performed the radiative transfer simulations, analyzed the data, and drafted the article. MW, AE, and CL designed the experimental basis of this study.

Competing interests. The authors declare that they have no conflict of interest.

Acknowledgements. We gratefully acknowledge the funding by the Deutsche Forschungsgemeinschaft (DFG, German Research Foundation) – Project Number 268020496 – TRR 172, within the Transregional Collaborative Research Center "ArctiC Amplification: Climate Relevant Atmospheric and SurfaCe Processes, and Feedback Mechanisms (AC)^3". The authors are grateful to AWI for providing and operating the two aircraft during the ACLOUD and AFLUX campaign. We thank the crews of Polar 5 and Polar 6, the technicians of the aircraft for excellent technical and logistical support. The generous funding of the flight hours for ACLOUD by AWI is greatly appreciated. Data provided by NCAR/EOL under the sponsorship of the National Science Foundation (https://data.eol.ucar.edu/). The authors acknowledge support from Stephen Hudson and Lana Cohen at the Norwegian Polar Institute and Von P. Walden at Washington State University for use of the N-ICE2015 dataset.

https://doi.org/10.5194/acp-2021-279
Preprint. Discussion started: 26 April 2021

Atmospheric Chemistry and Physics Discussions

References

Achtert, P., O'Connor, E. J., Brooks, I. M., Sotiropoulou, G., Shupe, M. D., Pospichal, B., Brooks, B. J., and Tjernström, M.: Properties of Arctic liquid and mixed-phase clouds from shipborne Cloudnet observations during ACSE 2014, Atmos. Chem. Phys., 20, 14 983–15 002, https://doi.org/10.5194/acp-20-14983-2020, 2020.

Becker, S., Ehrlich, A., Stapf, J., Lüpkes, C., Mech, M., Crewell, S., and Wendisch, M.: Meteorological measurements by dropsondes released from POLAR 5 during AFLUX 2019, PANGAEA, https://doi.org/10.1594/PANGAEA.921996, 2020.

Bennartz, R., Shupe, M. D., Turner, D. D., Walden, V. P., Steffen, K., Cox, C. J., Kulie, M. S., Miller, N. B., and Pettersen, C.: July 2101 Greenland melt extent enhanced by low–level liquid clouds, Nature, 496, 83–86, 2013.

Benner, T. C., Curry, J. A., and Pinto, J. O.: Radiative transfer in the summertime Arctic, J. Geophys. Res., 106, 15.173–15.183, 2001.

Binder, H., Boettcher, M., Grams, C. M., Joos, H., Pfahl, S., and Wernli, H.: Exceptional Air Mass Transport and Dynamical Drivers of an Extreme Wintertime Arctic Warm Event, Geophys. Res. Lett., 44, 12 028–12 036, https://doi.org/10.1002/2017GL075841, 2017.

Block, K., Schneider, F. A., Mülmenstädt, J., Salzmann, M., and Quaas, J.: Climate models disagree on the sign of total radiative feedback in the Arctic, Tellus A, 72, 1–14, https://doi.org/10.1080/16000870.2019.1696139, 2020.

Brümmer, B.: Boundary-layer modification in wintertime cold-air outbreaks from the arctic sea ice, Bound.-Layer Meteor., 80, 109–125, https://doi.org/10.1007/BF00119014, 1996.

Brümmer, B.: Boundary layer mass, water, and heat budgets in wintertime cold-air outbreaks from the Arctic sea ice, Monthly Weather Review, 125, 1824–1837, https://doi.org/10.1175/1520-0493(1997)125<1824:BLMWAH>2.0.CO;2, 1997.

Cesana, G., Kay, J. E., Chepfer, H., English, J. M., and de Boer, G.: Ubiquitous low-level liquid-containing Arctic clouds: New observations and climate model constraints from CALIPSO-GOCCP, Geophys. Res. Lett., 39, L20 804, https://doi.org/10.1029/2012GL053385, 2012.

Chechin, D. G. and Lüpkes, C.: Boundary-Layer Development and Low-level Baroclinicity during High-Latitude Cold-Air Outbreaks: A Simple Model, Bound.-Layer Meteor., 162, 91–116, https://doi.org/10.1007/s10546-016-0193-2, 2017.

Chechin, D. G., Lüpkes, C., Repina, I. A., and Gryanik, V. M.: Idealized dry quasi 2-D mesoscale simulations of cold-air outbreaks over the marginal sea ice zone with fine and coarse resolution, J. Geophys. Res., 118, 8787–8813, https://doi.org/10.1002/jgrd.50679, 2013.

Cohen, L., Hudson, S. R., Walden, V. P., Graham, R. M., and Granskog, M. A.: Meteorological conditions in a thinner Arctic sea ice regime from winter to summer during the Norwegian Young Sea Ice expedition (N-ICE2015), J. Geophys. Res., 122, 7235–7259, https://doi.org/10.1002/2016JD026034, 2017.

Cox, C. J., Walden, V. P., Rowe, P. M., and Shupe, M. D.: Humidity trends imply increased sensitivity to clouds in a warming Arctic, Nat. Commun., 6, 10 117, https://doi.org/10.1038/ncomms10117, 2015.

Cox, C. J., Morris, S. M., Uttal, T., Burgener, R., Hall, E., Kutchenreiter, M., McComiskey, A., Long, C. N., Thomas, B. D., and Wendell, J.: The De-Icing Comparison Experiment (D-ICE): a study of broadband radiometric measurements under icing conditions in the Arctic, Atmos. Meas. Tech., 14, 1205–1224, https://doi.org/10.5194/amt-14-1205-2021, 2021.

Ebell, K., Nomokonova, T., Maturilli, M., and Ritter, C.: Radiative Effect of Clouds at Ny-Ålesund, Svalbard, as Inferred from Ground-Based Remote Sensing Observations, J. Appl. Meteorol., 59, 3–22, https://doi.org/10.1175/JAMC-D-19-0080.1, 2020.

Ehrlich, A., Stapf, J., Lüpkes, C., Mech, M., Crewell, S., and Wendisch, M.: Meteorological measurements by dropsondes released from POLAR 5 during ACLOUD 2017, PANGAEA, https://doi.org/10.1594/PANGAEA.900204, 2019a.

Ehrlich, A., Wendisch, M., Lüpkes, C., Buschmann, M., Bozem, H., Chechin, D., Clemen, H.-C., Dupuy, R., Eppers, O., Hartmann, J., Herber, A., Jäkel, E., Järvinen, E., Jourdan, O., Kästner, U., Kliesch, L.-L., Köllner, F., Mech, M., Mertes, S., Neuber, R., Ruiz-

https://doi.org/10.5194/acp-2021-279
Preprint. Discussion started: 26 April 2021

Atmospheric Chemistry and Physics Discussions

Donoso, E., Schnaiter, M., Schneider, J., Stapf, J., and Zanatta, M.: A comprehensive in situ and remote sensing data set from the Arctic CLoud Observations Using airborne measurements during polar Day (ACLOUD) campaign, Earth Syst. Sci. Data, 11, 1853–1881, https://doi.org/10.5194/essd-11-1853-2019, 2019b.

Emde, C., Buras-Schnell, R., Kylling, A., Mayer, B., Gasteiger, J., Hamann, U., Kylling, J., Richter, B., Pause, C., Dowling, T., and Bugliaro, L.: The libRadtran software package for radiative transfer calculations (version 2.0.1), Geosci. Model Dev., 9, 1647–1672, https://doi.org/10.5194/gmd-9-1647-2016, 2016.

Fitzpatrick, M. F. and Warren, S. G.: The relative importance of clouds and sea ice for the solar energy budget of the Southern Ocean, J. Climate, 20, 941–954, https://doi.org/10.1175/JCLI4040.1, 2007.

Frey, W. R., Morrison, A. L., Kay, J. E., Guzman, R., and Chepfer, H.: The Combined Influence of Observed Southern Ocean Clouds and Sea Ice on Top-of-Atmosphere Albedo, J. Geophys. Res., 123, 4461–4475, https://doi.org/10.1029/2018JD028505, 2018.

Gardner, A. S. and Sharp, M. J.: A review of snow and ice albedo and the development of a new physically based broadband albedo parameterization, J. Geophys. Res., 115, F01 009, https://doi.org/10.1029/2009JF001444, 2010.

Goosse, H., Kay, J. E., Armour, K. C., Bodas-Salcedo, A., Chepfer, H., Docquier, D., Jonko, A., Kushner, P. J., Lecomte, O., Massonnet, F., Park, H. S., Pithan, F., Svensson, G., and Vancoppenolle, M.: Quantifying climate feedbacks in polar regions, Nat. Commun., 9, 1919, https://doi.org/10.1038/s41467-018-04173-0, 2018.

Graham, R. M., Rinke, A., Cohen, L., Hudson, S. R., Walden, V. P., Granskog, M. A., Dorn, W., Kayser, M., and Maturilli, M.: A comparison of the two Arctic atmospheric winter states observed during N-ICE2015 and SHEBA, J. Geophys. Res., 122, 5716–5737, https://doi.org/10.1002/2016JD025475, 2017.

Graham, R. M., Cohen, L., Ritzhaupt, N., Segger, B., Graversen, R. G., Rinke, A., Walden, V., Granskog, M. A., and Hudson, S. R.: Evaluation of Six Atmospheric Reanalyses over Arctic Sea Ice from Winter to Early Summer, J. Climate, 32, 4121–4143, https://doi.org/10.1175/JCLI-D-18-0643.1, 2019.

Gryschka, M., Fricke, J., and Raasch, S.: On the impact of forced roll convection on vertical turbulent transport in cold air outbreaks, J. Geophys. Res., 119, 12 513–12 532, https://doi.org/10.1002/2014JD022160, 2014.

Hartmann, J., Kottmeier, C., and Wamser, C.: Radiation and Eddy Flux Experiment 1991 (REFLEX I), Berichte zur Polarforschung, 105, 1992.

Hartmann, J., Lüpkes, C., and Chechin, D.: High resolution aircraft measurements of wind and temperature during the ACLOUD campaign in 2017, PANGAEA, https://doi.pangaea.de/10.1594/PANGAEA.900880, 2019.

Hersbach, H., Bell, B., Berrisford, P., Biavati, G., Horányi, A., Muñoz Sabater, J., Nicolas, J., Peubey, C., Radu, R., Rozum, I., Schepers, D., Simmons, A., Soci, C., Dee, D., and Thépaut, J.-N.: ERA5 hourly data on single levels from 1979 to present, Copernicus Climate Change Service (C3S) Climate Data Store (CDS), (Accessed on < 08-03-2021 >), https://doi.org/10.24381/cds.adbb2d47, 2018a.

Hersbach, H., Bell, B., Berrisford, P., Biavati, G., Horányi, A., Muñoz Sabater, J., Nicolas, J., Peubey, C., Radu, R., Rozum, I., Schepers, D., Simmons, A., Soci, C., Dee, D., and Thépaut, J.-N.: ERA5 hourly data on pressure levels from 1979 to present, Copernicus Climate Change Service (C3S) Climate Data Store (CDS), (Accessed on < 08-03-2021 >), https://doi.org/10.24381/cds.bd0915c6, 2018b.

Hersbach, H., Bell, B., Berrisford, P., Hirahara, S., Horányi, A., Muñoz-Sabater, J., Nicolas, J., Peubey, C., Radu, R., Schepers, D., Simmons, A., Soci, C., Abdalla, S., Abellan, X., Balsamo, G., Bechtold, P., Biavati, G., Bidlot, J., Bonavita, M., De Chiara, G., Dahlgren, P., Dee, D., Diamantakis, M., Dragani, R., Flemming, J., Forbes, R., Fuentes, M., Geer, A., Haimberger, L., Healy, S., Hogan, R. J., Holm, E., Janiskova, M., Keeley, S., Laloyaux, P., Lopez, P., Lupu, C., Radnoti, G., de Rosnay, P., Rozum, I., Vamborg, F., Villaume, S., and Thépaut, J. N.: The ERA5 global reanalysis, Quart. J. Roy. Meteor. Soc., 146, 1999–2049, https://doi.org/10.1002/qj.3803, 2020.

https://doi.org/10.5194/acp-2021-279
Preprint. Discussion started: 26 April 2021

Atmospheric Chemistry and Physics Discussions

Hudson, S. R., Cohen, L., and Walden, V. P.: N-ICE2015 surface broadband radiation data, Norwegian Polar Institute, https://doi.org/10.21334/npolar.2016.a89cb766, 2016.

Hudson, S. R., Cohen, L., Kayser, M., Maturilli, M., Kim, J.-H., Park, S.-J., Moon, W., and Granskog, M. A.: N-ICE2015 atmospheric profiles from radiosondes [Data set], Norwegian Polar Institute, https://doi.org/10.21334/npolar.2017.216df9b3, 2017.

Jin, Z. H., Qiao, Y. L., Wang, Y. J., Fang, Y. H., and Yi, W. N.: A new parameterization of spectral and broadband ocean surface albedo, Opt. Express, 19, 26 429–26 443, https://doi.org/10.1364/OE.19.026429, 2011.

Karlsson, J. and Svensson, G.: Consequences of poor representation of Arctic sea-ice albedo and cloud-radiation interactions in the CMIP5 model ensemble, Geophys. Res. Lett., 40, 4374–4379, https://doi.org/10.1002/grl.50768, 2013.

Kayser, M., Maturilli, M., Graham, R. M., Hudson, S. R., Rinke, A., Cohen, L., Kim, J. H., Park, S. J., Moon, W., and Granskog, M. A.: Vertical thermodynamic structure of the troposphere during the Norwegian young sea ICE expedition (N-ICE2015), J. Geophys. Res., 122, 10 855–10 872, https://doi.org/10.1002/2016JD026089, 2017.

Knudsen, E. M., Heinold, B., Dahlke, S., Bozem, H., Crewell, S., Gorodetskaya, I. V., Heygster, G., Kunkel, D., Maturilli, M., Mech, M., Viceto, C., Rinke, A., Schmithüsen, H., Ehrlich, A., Macke, A., Lüpkes, C., and Wendisch, M.: Meteorological conditions during the ACLOUD/PASCAL field campaign near Svalbard in early summer 2017, Atmos. Chem. Phys., 18, 17 995–18 022, https://doi.org/10.5194/acp-18-17995-2018, 2018.

Koenigk, T., Key, J., and Vihma, T.: Climate Change in the Arctic, pp. 673–705, Springer International Publishing, Cham, https://doi.org/10.1007/978-3-030-33566-3_11, 2020.

Lampert, A., Maturilli, M., Ritter, C., Hoffmann, A., Stock, M., Herber, A., Birnbaum, G., Neuber, R., Dethloff, K., Orgis, T., Stone, R., Brauner, R., Kassbohrer, J., Haas, C., Makshtas, A., Sokolov, V., and Liu, P.: The spring-time boundary layer in the central Arctic observed during PAMARCMiP 2009, Atmosphere-Basel, 3, 320–351, https://doi.org/10.3390/atmos3030320, 2012.

Maturilli, M.: High resolution radiosonde measurements from station Ny-Ålesund (2017-04 et seq), Alfred Wegener Institute - Research Unit Potsdam, PANGAEA, https://doi.org/10.1594/PANGAEA.914973, 2020.

Meier, W. N., Hovelsrud, G. K., van Oort, B. E., Key, J. R., Kovacs, K. M., Michel, C., Haas, C., Granskog, M. A., Gerland, S., Perovich, D. K., Makshtas, A., and Reist, J. D.: Arctic sea ice in transformation: A review of recent observed changes and impacts on biology and human activity, Reviews of Geophysics, 52, 185–217, http://dx.doi.org/10.1002/2013RG000431, 2013RG000431, 2014.

Mewes, D. and Jacobi, C.: Heat transport pathways into the Arctic and their connections to surface air temperatures, Atmos. Chem. Phys., 19, 3927–3937, https://doi.org/10.5194/acp-19-3927-2019, 2019.

Miller, N. B., Shupe, M. D., Cox, C. J., Walden, V. P., Turner, D. D., and Steffen, K.: Cloud Radiative Forcing at Summit, Greenland, J. Climate, 28, 6267–6280, https://doi.org/10.1175/JCLI-D-15-0076.1, 2015.

Mioche, G., Jourdan, O., Delanoe, J., Gourbeyre, C., Febvre, G., Dupuy, R., Monier, M., Szczap, F., Schwarzenboeck, A., and Gayet, J. F.: Vertical distribution of microphysical properties of Arctic springtime low-level mixed-phase clouds over the Greenland and Norwegian seas, Atmos. Chem. Phys., 17, 12 845–12 869, https://doi.org/10.5194/acp-17-12845-2017, 2017.

Moritz, R.: Soundings, Ice Camp NCAR/GLAS raobs. (ASCII). Version 2.0, UCAR/NCAR - Earth Observing Laboratory, https://doi.org/https://doi.org/10.5065/D6FQ9V0Z, 2017.

Papritz, L. and Spengler, T.: A Lagrangian Climatology of Wintertime Cold Air Outbreaks in the Irminger and Nordic Seas and Their Role in Shaping Air-Sea Heat Fluxes, J. Climate, 30, 2717–2737, https://doi.org/10.1175/JCLI-D-16-0605.1, 2017.

Persson, P. O. G.: SHEBA Composite Data Observations. Version 1.0. UCAR/NCAR - Earth Observing Laboratory, https://doi.org/https://doi.org/10.5065/D6PN93R6, 2011.

https://doi.org/10.5194/acp-2021-279
Preprint. Discussion started: 26 April 2021

Atmospheric Chemistry and Physics Discussions

Persson, P. O. G., Shupe, M. D., Perovich, D., and Solomon, A.: Linking atmospheric synoptic transport, cloud phase, surface energy fluxes, and sea-ice growth: observations of midwinter SHEBA conditions, Climate Dyn., 49, 1341–1364, https://doi.org/10.1007/s00382-016-3383-1, 2017.

Pithan, F. and Mauritsen, T.: Arctic amplification dominated by temperature feedbacks in contemporary climate models, Nature, 7, 181–184, https://doi.org/10.1038/ngeo2071, 2014.

Pithan, F., Medeiros, B., and Mauritsen, T.: Mixed-phase clouds cause climate model biases in Arctic wintertime temperature inversions, Climate Dyn., 43, 289–303, https://doi.org/10.1007/s00382-013-1964-9, 2014.

Pithan, F., Svensson, G., Caballero, R., Chechin, D., Cronin, T. W., Ekman, A. M. L., Neggers, R., Shupe, M. D., Solomon, A., Tjernström, M., and Wendisch, M.: Role of air-mass transformations in exchange between the Arctic and mid-latitudes, Nat. Geosci., 11, 805–812, https://doi.org/10.1038/s41561-018-0234-1, 2018.

Ramanathan, V., Cess, R, D., Harrison, E. F., Minnis, P., Barkstrom, B. R., Ahmad, E., and Hartmann, D.: Cloud-radiative forcing and climate: Results from the Earth Radiation Budget Experiment, Science, 243, 57–63, 1989.

Rolph, R. J., Feltham, D. L., and Schröder, D.: Changes of the Arctic marginal ice zone during the satellite era, Cryosphere, 14, 1971–1984, https://doi.org/10.5194/tc-14-1971-2020, 2020.

Schmithüsen, H.: Upper air soundings during POLARSTERN cruise PS106.1 (ARK-XXXI/1.1), PANGAEA, https://doi.org/10.1594/PANGAEA.882736, 2017.

Screens, J. A. and Simmonds, I.: The central role of diminishing sea ice in recent Arctic temperature amplification, Nature, 464, 1334–1337, 2010.

Sedlar, J., Tjernstrom, M., Mauritsen, T., Shupe, M. D., Brooks, I. M., Persson, P. O. G., Birch, C. E., Leck, C., Sirevaag, A., and Nicolaus, M.: A transitioning Arctic surface energy budget: the impacts of solar zenith angle, surface albedo and cloud radiative forcing, Climate Dyn., 37, 1643–1660, https://doi.org/10.1007/s00382-010-0937-5, 2011.

Sedlar, J., Tjernstrom, M., Rinke, A., Orr, A., Cassano, J., Fettweis, X., Heinemann, G., Seefeldt, M., Solomon, A., Matthes, H., Phillips, T., and Webster, S.: Confronting Arctic Troposphere, Clouds, and Surface Energy Budget Representations in Regional Climate Models With Observations, Journal of Geophysical Research-atmospheres, 125, e2019JD031 783, https://doi.org/10.1029/2019JD031783, 2020.

Shupe, M. D. and Intrieri, J. M.: Cloud radiative forcing of the Arctic surface: The influence of cloud properties, surface albedo, and solar zenith angle, J. Climate, 17, 616–628, 2004.

Spreen, G., Kaleschke, L., and Heygster, G.: Sea ice remote sensing using AMSR-E 89-GHz channels, J. Geophys. Res., 113, C02S03, https://doi.org/10.1029/2005JC003384, 2008.

Stapf, J., Ehrlich, A., Jäkel, E., and Wendisch, M.: Aircraft measurements of broadband irradiance during the ACLOUD campaign in 2017, PANGAEA, https://doi.org/10.1594/PANGAEA.900442, 2019.

Stapf, J., Ehrlich, A., Jäkel, E., Lüpkes, C., and Wendisch, M.: Reassessment of shortwave surface cloud radiative forcing in the Arctic: consideration of surface-albedo–cloud interactions, Atmos. Chem. Phys., 20, 9895–9914, https://doi.org/10.5194/acp-20-9895-2020, 2020.

Stapf, J., Ehrlich, A., and Wendisch, M.: Influence of Thermodynamic State Changes on Surface Cloud Radiative Forcing in the Arctic: A Comparison of Two Approaches Using Data From AFLUX and SHEBA, J. Geophys. Res., 126, e2020JD033 589, https://doi.org/10.1029/2020JD033589, 2021.

Stramler, K., Del Genio, A. D., and Rossow, W. B.: Synoptically Driven Arctic Winter States, J. Climate, 24, 1747–1762, https://doi.org/10.1175/2010JCLI3817.1, 2011.

https://doi.org/10.5194/acp-2021-279
Preprint. Discussion started: 26 April 2021

Stroeve, J. and Notz, D.: Changing state of Arctic sea ice across all seasons, Environ. Res. Lett., 13, 103 001, https://doi.org/10.1088/1748-9326/aade56, 2018.

Tetzlaff, A., Lüpkes, C., Birnbaum, G., Hartmann, J., Nygård, T., and Vihma, T.: Brief Communication: Trends in sea ice extent north of Svalbard and its impact on cold air outbreaks as observed in spring 2013, Cryosphere, 8, 1757–1762, https://doi.org/10.5194/tc-8-1757-2014, 2014.

Tetzlaff, A., Lüpkes, C., and Hartmann, J.: Aircraft-based observations of atmospheric boundary-layer modification over Arctic leads, Quart. J. Roy. Meteor. Soc., 141, 2839–2856, https://doi.org/10.1002/qj.2568, 2015.

Tjernström, M., Shupe, M. D., Brooks, I. M., Persson, P. O. G., Prytherch, J., Salisbury, D. J., Sedlar, J., Achtert, P., Brooks, B. J., Johnston, P. E., Sotiropoulou, G., and Wolfe, D.: Warm-air advection, air mass transformation and fog causes rapid ice melt, Geophys. Res. Lett., 42, 5594–5602, https://doi.org/10.1002/2015GL064373, 2015.

Tjernström, M., Shupe, M. D., Brooks, I. M., Achtert, P., Prytherch, J., and Sedlar, J.: Arctic Summer Airmass Transformation, Surface Inversions, and the Surface Energy Budget, J. Climate, 32, 769–789, https://doi.org/10.1175/JCLI-D-18-0216.1, 2019.

Uttal, T., Curry, J. A., McPhee, M. G., Perovich, D. K., Moritz, R. E., Maslanik, J. A., Guest, P. S., Stern, H. L., Moore, J. A., Turenne, R., Heiberg, A., Serreze, M. C., Wylie, D. P., Persson, O. G., Paulson, C. A., Halle, C., Morison, J. H., Wheeler, P. A., Makshtas, A., Welch, H., Shupe, M. D., Intrieri, J. M., Stamnes, K., Lindsey, R. W., Pinkel, R., Pegau, W. S., Stanton, T. P., and Grenfeld, T. C.: Surface heat budget of the Arctic Ocean, B. Am. Meteorol. Soc., 83, 255–275, https://doi.org/10.1175/1520-0477(2002)083<0255:SHBOTA>2.3.CO;2, 2002.

Vihma, T., Pirazzini, R., Fer, I., Renfrew, I. A., Sedlar, J., Tjernström, M., Lüpkes, C., Nygård, T., Notz, D., Weiss, J., Marsan, D., Cheng, B., Birnbaum, G., Gerland, S., Chechin, D., and Gascard, J. C.: Advances in understanding and parameterization of small-scale physical processes in the marine Arctic climate system: a review, Atmos. Chem. Phys., 14, 9403–9450, https://doi.org/10.5194/acp-14-9403-2014, 2014.

Walden, V. P., Hudson, S. R., Cohen, L., Murphy, S. Y., and Granskog, M. A.: Atmospheric components of the surface energy budget over young sea ice: Results from the N-ICE2015 campaign, J. Geophys. Res., 122, 8427–8446, https://doi.org/10.1002/2016JD026091, 2017.

Wendisch, M., Müller, D., Schell, D., and Heintzenberg, J.: An airborne spectral albedometer with active horizontal stabilization, J. Atmos. Oceanic Technol., 18, 1856–1866, 2001.

Wendisch, M., Brückner, M., Burrows, J. P., Crewell, S., Dethloff, K., Ebell, K., Lüpkes, C., Macke, A., Notholt, J., Quaas, J., Rinke, A., and Tegen, I.: Understanding causes and effects of rapid warming in the Arctic, Eos, 98, https://doi.org/10.1029/2017EO064803, 2017.

Wendisch, M., Macke, A., Ehrlich, A., Lüpkes, C., Mech, M., Chechin, D., Barrientos, C., Bozem, H., Brückner, M., Clemen, H.-C., Crewell, S., Donth, T., Dupuy, R., Ebell, K., Egerer, U., Engelmann, R., Engler, C., Eppers, O., Gehrmann, M., Gong, X., Gottschalk, M., Gourbeyre, C., Griesche, H., Hartmann, J., Hartmann, M., Herber, A., Herrmann, H., Heygster, G., Hoor, P., Jafariserajehlou, S., Jäkel, E., Järvinen, E., Jourdan, O., Kästner, U., Kecorius, S., Knudsen, E. M., Köllner, F., Kretzschmar, J., Lelli, L., Leroy, D., Maturilli, M., Mei, L., Mertes, S., Mioche, G., Neuber, R., Nicolaus, M., Nomokonova, T., Notholt, J., Palm, M., van Pinxteren, M., Quaas, J., Richter, P., Ruiz-Donoso, E., Schäfer, M., Schmieder, K., Schnaiter, M., Schneider, J., Schwarzenböck, A., Seifert, P., Shupe, M. D., Siebert, H., Spreen, G., Stapf, J., Stratmann, F., Vogl, T., Welti, A., Wex, H., Wiedensohler, A., Zanatta, M., and Zeppenfeld, S.: The Arctic cloud puzzle: using ACLOUD/PASCAL multi-platform observations to unravel the role of clouds and aerosol particles in Arctic amplification, B. Am. Meteorol. Soc., 100 (5), 841–871, https://doi.org/10.1175/BAMS-D-18-0072.1, 2019.

Yamanouchi, T.: Arctic warming by cloud radiation enhanced by moist air intrusion observed at Ny-Ålesund, Svalbard, Polar Sci., 21, 110–116, https://doi.org/10.1016/j.polar.2018.10.009, 2019.

https://doi.org/10.5194/acp-2021-279
Preprint. Discussion started: 26 April 2021

Atmospheric Chemistry and Physics Discussions

Zatko, M. C. and Warren, S. G.: East Antarctic sea ice in spring: spectral albedo of snow, nilas, frost flowers and slush, and light-absorbing impurities in snow, Ann. Glaciol., 56, 53–64, https://doi.org/10.3189/2015AoG69A574, 2015.

Zygmuntowska, M., Mauritsen, T., Quaas, J., and Kaleschke, L.: Arctic Clouds and Surface Radiation - a critical comparison of satellite retrievals and the ERA-Interim reanalysis, Atmos. Chem. Phys., 12, 6667–6677, https://doi.org/10.5194/acp-12-6667-2012, 2012.